Swift, C. T. & McIntosh, R. E. 1983 Considerations for microwave remote sensing of ocean-surface salinity, IEEE Trans. Geosci. Remote Sensing, 21, 480-491.

Takahashi, T., R. A. Feely, R. F. Weiss, R. Wanninkhof, D. W. Chipman, S. C. Sutherland, T. T. Takahashi 1997: Global air-sea flux of CO_2: An estimate based on measurements of air-sea pCO_2 difference, Proc. Natl. Acad. Sci. USA, 94, 8292-8299.

Timmermann, A., M. Latif, R. Voss, A. Grötzner, 1998: North Atlantic Variability: a coupled air-sea mode, J. Climate, 11, 1906-1931.

Trites, R.W., 1982: Overview of oceanographic conditions in NAFO Subareas 2, 3, and 4 during the 1970-79 decade, Northwest Atlantic Fisheries Organisation, Scientific Counsil Studies, 5, 51-78.

van Aken, H.M., G. Budeús, M. Hähnel, 1995: The anatomy of the Arctic Frontal Zone in the Greenland Sea, J. Geophys. Res., 100, 15999-16014.

Vialard, J., P. Delecluse, 1998a: An OGCM study for the TOGA decade. Part I: Role of the salinity in the physics of the western Pacific fresh pool, J. Phys. Oceanog., 28, 1071-1088.

Vialard, J., P. Delecluse, 1998b: An OGCM study for the TOGA decade. Part II: Barrier-layer formation and variability, J. Phys. Oceanog., 28, 1089-1106.

Wallace, J.M., E.M. Rasmusson, T.P. Mitchell, V.E. Kousky, E.S. Sarachik, H. von Storch, 1998: On the structure and evolution of ENSO-related climate variability in the tropical Pcific: Lessons from TOGA, J. Geophys. Res., 103, 14241-14259.

Webster, P.J., 1994: The role of hydrological processes in ocean-atmosphere interactions, Rev. Geophys., 32, 427-476.

Webster, W.J., T.T. Wilheit, 1976: Spectral characteristics of the microwave emission from a wind-driven foam-covered sea, J. Geophys. Res., 81, 3095-3099.

Weiss, R. F., 1974: Carbon dioxide in water and seawater: The solubility of a non-ideal gas, Mar. Chem., 2, 203-215.

Wijsekera, H., C.A. Paulson, A. Huyer, 1998: The effect of rainfall on the surface layer during a westerly wind burst in the western equatorial Pacific, J. Phys. Oceanog., in press.

Rossby, T., 1996: The North Atlantic Current and surrounding watres at the crossroads, Rev. geophys., 34, 463-481.

Rudels, B., 1990: Haline convection in the Greenland Sea, Deep-Sea Res., Part A, 37, 1491-1511.

Schauer, U., 1995: The release of brine-enriched shelf water from Storfjord into the Norwegian Sea, J. Geophys. Res., 100, 16015-16028.

Schlüssel, P., W.J. Emery, 1990: Atmospheric water vapour over oceans from SSM/I measurements, Int. J. Remote Sensing, 11, 753-760.

Schlüssel, P., A.V. Soloviev, W.J. Emery, 1997: Cool and freshwater skin of the ocean during rainfall, Boundary-Layer Meteor., 82, 437-472.

Schott, F., M. Visbeck, J. Fischer, 1993: Observations of vertical currents and convection in the central Greenland Sea during the winter 1988/89, J. geophys. Res., 98, 14401-14421.

Semtner, A. J., 1995 Modelling ocean circulation, Science, 269, 1379-1385.

Shinoda, T., R. Lukas, 1995: Lagrangian mixed layer modelling of the western equatorial pacific, J. Geophys. Res., 100, 2523-2541.

Siefridt, L. & Barnier, B. 1993 Banque de Donnees AVISO Vent/flux: Climatologie des Analyses de Surface de CEPMMT, Report 91 1430 025, AVISO, 43pp.

Skou, N. 1995 An overview of requirements and passive microwave radiometer options, pp.41-48 in Consultative meeting on Soil Moisture and Ocean Salinity measurement requirements and radiometer techniques (SMOS), Noordwijk, 1995, WPP-87, ESA.

Smith, N., 1997: The global ocean data assimilation experiment (GODAE), http://www.bom.gov.au/bmcr/nrs/oopc/godae/3pager.htm.

Guissard, A., Sobieski, P., Laloux, A., 1994: Radiative transfer equation with surface scattering for ocean and atmospheric parameters retrieval from radiometric measurements, Int. J. remote Sensing, 15, 1743-1760.

Soloviev, A.V., R. Lukas, 1997: Sharp frontal interfaces in near-surface layer of the ocean in the western equatorial Pacific warm pool, J. Phys. Oceanog., 27, 999-1017.

Srokosz, M. A. 1995 Ocean surface salinity - the why, what and whether, pp.49-56 in Consultative meeting on Soil Moisture and Ocean Salinity measurement requirements and radiometer techniques (SMOS), Noordwijk, 1995, WPP-87, ESA.

Sprintall, J., M. Tomczak, 1992: Evidence of the barrier layer in the surface layer of the tropics, J. Geophys. Res., 97, 7305-7316.

Swift, C. T. 1993 ESTAR - the Electronically Scanned Thinned Array Radiometer for remote sensing measurement of soli moisture and ocean salinity, NASA Technical Memorandum TM-4523, NASA, 40 pp.

Lukas, R., 1989: Freshwater input on the western equatorial ocean and air-sea interaction, Proc. Symp. Western Trop. Pacific Air-Sea Interactions, Beijing, 15-17 November 1988.

Lukas, R., 1990: The role of salinity in the dynamics and thermodynamics of the western Pacific warm pool, In: Proc. Int. TOGA Sci. Conf., 16-20 July 1990, Honolulu, Hawaii.

Lukas, R., E. Lindstrom, 1991: The mixed layer of the western equatorial Pacific ocean, J. Geophys. Res., 96, 3343-3357.

Martin, J.H.A., H.D. Dooley, W. Shearer, 1984: Ideas on the origin and biological consequences of the 1970s salinity anomaly, International Council for the Exploration of the Sea, Contributions to Counsil Meetings CM 1984, Gen. 18, 7pp + 12 figs.

McPhaden, M.J., A.J. Busalacchi, R. Cheney, j.-R. Donguy, K.S. Gage, D. Halpern, M. Ji, P. Julian, G. Meyers, G.T. Mitchum, P.P. Niiler, J. Picaut, R.W. Reynolds, N. Smith, K. Takeuchi, 1998: The Tropical Ocean-Global Atmosphere observing system: A decade of progress, J. Geophys. Res. 103, 14169-14249.

Miller, J.L., M.A. Goodberlet, J.B. Zaitzeff, 1998: Airborne salinity maper makes debut in coastal zone, Eos - Trans. AGU, 79, 173 and 176-177.

Miller, J.R., 1976: The salinity effect in a mixed layer ocean model, J. Phys. Oceanog., 6, 29-35.

Mitchell, J.F.B., K.W. Dixon, 1997: Initialisation of coupled models for use in climate studies, 1st Session Report of JSC/Clivar Working Group on coupled modelling, Appendix D, available from Int. CLIVAR Project Office.

Pandey, P.C., R.K. Kakar, 1982: An empirical microwaves emissivity model for a foam-covered sea, IEEE J. Ocean Eng., 7, 135-140.

Paulson, C.A., G.S.E. Lagerloef, 1993: Fresh surface lenses caused by heavy rain over the western pacific warm pool during TOGA COARE, Eos, Trans. AGU, 74, Suppl. to Nr. 43, 125.

Picaut, J., M. Ioulalen, T. Delcroix, M.J. McPhaden, C. Menkes, 1996: Mechanism of the zonal displacements of the Pacific warm pool: Implications for ENSO, Science, 274, 1486-1489.

Pollard, R.T., S. Pu, 1985: Structure and circulation of the upper Atlantic Ocean northeast of the Azores, Prog. Oceanog., 14, 443-462.

Price, J.F., 1979: Observations of a rain-formed mixed layer, J. Phys. Oceanog., 9, 643-649.

Price, J.F., R. Weller, R. Pinkel, 1986: Diurnal cycling: Observations and models of upper ocean response to diurnal heating, cooling and wind mixing, J. Geophys. Res., 91, 8411-8427.

Godfrey, J.S., R.A. Houze Jr., R.H. Johnson, R. Lukas, J.-L. Redelsperger, A. Sumi, R. Weller, 1998: Coupled ocean-atmosphere response experiment (COARE): An interim report, J. Geophys. Res., 103, 14395-14450.

Goutoule, J. M. 1995 MIRAS space borne instrument, and its airborne demonstrator, pp.65-69 in Consultative meeting on Soil Moisture and Ocean Salinity measurement requirements and radiometer techniques (SMOS), Noordwijk, 1995, WPP-87, ESA.

Haney, R. L, 1971 Surface thermal boundary condition for ocean circulation models, J. Phys. Oceanogr., 1, 241-248.

Hollinger, J. P. 1971 Passive microwave measurements of sea surface roughness, IEEE Trans. Geosci. Remote Sensing, 9, 165-169.

Hughes, T.M., A.J. Weaver, 1996: Sea surface temperature-evaporation feedback and the ocean's thermohaline circulation, J. Phys. Oceanog., 26, 644-654.

IOC / WMO 1998 Final report: Workshop on the implementation of Global Ocean Observations for GOOS / GCOS, GOOS Report No. 64 / GCOS Report No. 49.

Kessler, W., B. Taft, 1987: Dynamic heights and zonal geostrophic transports in the central tropical Pacific during 1979-85, J. Phys. Oceanog., 17, 97-122.

Klein, L.A., C.T. Swift, 1977: An improved model for the dielectric constant of sea water at microwave frequencies, IEEE Trans. Antennas Propag., 25, 104-111.

Kourafalou, V.H., T.N. Lee, L.-J. Oey, J.D. Wang, 1996: The fate of river discharge on the continental shelf 2. Transport of coastal low-salinity waters under realistic wind and tidal forcing, J. Geophys. Res., 101, 3435-3455.

Kuroda, Y., M.J. McPhaden, 1993: Variability in the western equatorial Pacific Ocean during Japanese Pacific climate study cruises in 1989 and 1990, J. Geophys. Res., 98, 4747-4759.

Lagerloef, G.S.E., C.T. Swift, D.M. Le Vine, 1995: Sea Surface Salinity: The Next Remote Sensing Challenge, Oceanography, 8, 44-50.

Levitus, S., Boyer, T. P. 1994 World Ocean Atlas 1994 Volume 4: Temperature, NOAA Atlas NESDIS 4, NOAA, 117pp.

Levitus, S., R. Burgett, T.P. Boyer, 1994: NOAA Atlas NESDIS 3, World Ocean Atlas 1994 Volume 3: Salinity, U.S. Dept. Commerce, Washington, D.C., 99 pp.

Liebe, H.J., 1989: An atmospheric millimeter wave propagation model, Int. J. Infrared Millimeter Waves, 10, 631-650.

Lerner, R. M. & Hollinger, J. P. 1977 Analysis of 1.4GHz radiometric measurements from Skylab, Remote Sensing Env., 6, 251-269.

Brainerd, K.E., M.C. Gregg, 1997: Turbulence and stratification on the Tropical Ocean-Global Atmosphere –Coupled Ocean-Atmosphere Response Experiment microstructure pilot cruise, J. Geophys. Res., 102, 10437-10455.

Blume, H.-J. C., Kendall, B. M. & Fedors, J. C. 1978 Measurements of ocean temperature and salinity via microwave radiometry, Bound. Layer Met., 13, 295-308.

Chen, D.L., L.M. Rothstein, 1991: Modeling the mixed layer structures of the western equatorial Pacific, TOGA Notes, 2, 3-16, Oceanog. Center, Nova Southeastern Univ., Dania, FL.

Cooper, N.S., 1988: The effect of salinity on tropical ocean models, J. Phys. Oceanog., 18, 697-707.

Delecluse, P., M.K. Davey, Y. Kitamura, S.G.H. Philander, M. Suarez, L. Bengtsson, 1998: Coupled general circulation modeling of the tropical Pacific, J. Geophys. Res., 103, 14357-14373.

Delcroix, T., C. Hénin, 1991: Seasonal and interannual variations of sea surface salinity in the tropical Pacific Ocean, J. Geophys. Res., 96, 22135-22150.

Dessier, A., J.R. Donguy, 1987: Responses to El Niño signal of the epiplanktonic copepod population in the eastern tropical Pacific, J. Geophys. Res., 92, 14393-14403.

Dickson, R.R., J. Meincke, S.-A. Malmberg, A.J. Lee, 1988: The “Great Salinity Anomaly” in the Northern North Atlantic 1968-1982, Prog. Oceanog., 20, 101-151.

Doney, S.C., W.G. Large, F.O. Bryan, 1998: Surface ocean fluxes and water mass transformation rates in the coupled NCAR climate system model, J. Climate, 11, 1420-1441.

Donguy, J.-R., 1982: A climatic scenario in the western Pacific associated with El Niño event, Tropical Ocean-Atmosphere Newsletter, 13, 4-5.

Donguy, J.-R., 1994: Surface and subsurface salinity in the tropical Pacific Ocean. Relations with climate, Prog. Oceanog., 34, 45-78.

Drange, H., Simonsen, K, 1997 Formulation and spinup of the ESOP2 version of MICOM, Tech. Rep. #117, Nansen Environmental and Remote Sensing Center, Solheimsviken, Norway.

Droppelman, J.D., R.A. Mennella, D.E. Evans, 1970: An airborne measurement of the salinity variations of the Mississippi River outflow, J. Geophys. Res., 75, 5909-5913.

Dugdale, R. C., J. J. Goering, 1967: Uptake of new and regenerated forms of nitrogen in primary production, Limn. Oceanogr., 12, 196-206.

Eldin, G., M.H. Radenac, M. Rodier, 1998: Physical and nutrient variability in the upper equatorial Pacific associated with westerly wind forcing and wave activity, Deep-Sea Res., in press.

8.3 Acronyms

AOGCM	Atmosphere Ocean General Circulation Model
CGCM	Coupled General Circulation Model
CLIVAR	Climate Variability and Predictability
COARE	Coupled Ocean Atmosphere Response Experiment
ENSO	El Niño Southern Oscillation
GCOS	Global Climate Observing System
GIN Sea	Greenland-Iceland-Norwegian Sea
GLOBEC	Global Ocean Ecosystems Dynamics Program
GODAE	Global Ocean Data Assimilation Experiment
GOOS	Global Ocean Observing System
ITZC	Inner Tropical Convergence Zone
NEΔT	Noise Equivalent Temperature Difference
NCEP	National Centers for Environmental Prediction
OGCM	Ocean General Circulation Model
OOPC	Ocean Observations Panel for Climate
OS	Ocean Salinity
Psu	Practical salinity units
SSS	Sea Surface Salinity
SST	Sea Surface Temperature
SPCZ	South Pacific Convergence Zone
SURTROPAC	Surveillance Tropical Pacifique
TOGA	Tropical Ocean Global Atmosphere
WCRP	World Climate Research Programme
XBT	eXpandable Bathy-Thermograph

8.4 References

Anderson, S.P., R.A. Weller, R.B. Lukas, 1996: Surface buoyancy forcing and the mixed layer of the western Pacific warm pool: Observations and 1D model results, J. Climate, 9, 3056-3085.

Acero-Schertzer, C.E., D.V. Hansen, M.S. Swenson, 1997: Evaluation and diagnosis of surface currents in the National Centers for Environmental Prediction's ocean analyses, J. Geophys. Res., 102, 21037-21048.

Backhaus, J.O., H. Fohrmann, J. Kämpf, A. Rubino, 1997: Formation and export of water masses produced in Arctic shelf polynyas, ICES – J. Marine Sci., 54, 366-382.

Belkin, I.M., S. Levitus, J. Antonov, S.-A. Malmberg, 1998: "Great salinity anomalies" in the North Atlantic, Prog. Oceanog., 41, 1-68.

Bleck, R., C. Rooth, D. Hu, L. T. Smith, 1992 Salinity-driven thermocline transients in a wind- and thermohaline-forced isopycnic ccordinate model of the North Atlantic, J. Phys. Oceanogr., 22, 1482-1505.

$$\sigma(S,T) = \sigma(S,25)\ \exp(-\Delta\beta)$$

$$\Delta = 25 - T$$

$$\beta = 2.033 \text{ x } 10^{-2} + 1.266 \text{ x } 10^{-4}\,\Delta + 2.464 \text{ x } 10^{-6}\Delta^2 - S\gamma$$

$$\gamma = 1.849 \text{ x } 10^{-5} - 2.551 \text{ x } 10^{-7}\,\Delta + 2.551 \text{ x } 10^{-8}\Delta^2$$

$$\sigma(S,25) = S(0.182521 - 1.46192 \text{ x } 10^{-3}S + 2.09324 \text{ x } 10^{-5}S^2 - 1.28205 \text{ x } 10^{-7}S^3)$$

The above are the equations that have been used to relate the brightness temperature to the sea surface temperature and salinity, in the simulations of the retrieval of S using an L-band (f = 1.43GHz) passive microwave instrument.

$$T_b = e_{h,v} T$$

$$e_{h,v} = 1 - R_{h,v}$$

$$R_h = \left| \frac{\cos \vartheta_i - \sqrt{\varepsilon - \sin^2 \vartheta_i}}{\cos \vartheta_i + \sqrt{\varepsilon - \sin^2 \vartheta_i}} \right|^2$$

$$R_v = \left| \frac{\varepsilon \cos \vartheta_i - \sqrt{\varepsilon - \sin^2 \vartheta_i}}{\varepsilon \cos \vartheta_i + \sqrt{\varepsilon - \sin^2 \vartheta_i}} \right|^2$$

$$\varepsilon = \varepsilon_\infty + \frac{\varepsilon_s - \varepsilon_\infty}{1 + i\omega\tau} - i\frac{\sigma}{\omega\varepsilon_0}$$

Here $\omega = 2\pi f$ is where f is the frequency in Hz. $\varepsilon_\infty = 4.9$ is the dielectric constant at infinite frequency, ε_s is the static dielectric constant, τ is the relaxation time in seconds, σ is the ionic conductivity in mho per metre, and $\varepsilon_0 = 8.854 \text{ x } 10^{-12}$ is the permittivity of free space in Farads per metre. ε_s, τ and σ are all functions of the salinity S (in psu) and temperature T (in ˚C, except for the first equation above where it is in K). This dependence is given by the following equations.

$$\varepsilon_s(S,T) = \varepsilon_s(T)\, a(S,T)$$

$$\varepsilon_s(T) = 87.134 - 0.1949T + 1.276 \text{ x } 10^{-2} T^2 + 2.491 \text{ x } 10^{-4} T^3$$

$$a(S,T) = 1.000 + 1.613 \text{ x } 10^{-5} S\, T - 3.656 \text{ x } 10^{-3} S + 3.210 \text{ x } 10^{-5} S^2 - 4.232 \text{ x } 10^{-7} S^3$$

$$\tau(S,T) = \tau(0,T)\, b(S,T)$$

$$\tau(0,T) = 1.768 \text{ x } 10^{-11} - 6.086 \text{ x } 10^{-13} T + 1.104 \text{ x } 10^{-14} T^2 - 8.111 \text{ x } 10^{-17} T^3$$

$$b(S,T) = 1.000 + 2.282 \text{ x } 10^{-5} S\, T - 7.638 \text{ x } 10^{-4} S - 7.760 \text{ x } 10^{-6} S^2 + 1.105 \text{ x } 10^{-8} S^3$$

In addition, given that oceanographers traditionally work with bulk salinity and temperature, rather than surface values, consideration needs to be given to surface effects on the recovery of the salinity. For example, diurnal heating and cooling of the surface affects the sea surface temperature which is needed for the recovery, or the presence of a freshwater layer at the surface in regions of high rainfall will change the value of the sea surface salinity recovered. Effects such as these may lead to regional biases in salinity retrieval and need to investigate.

Finally, it should be noted that the results shown in section 4 represent a kind of a worst case scenario. No knowledge about the cross correlation, which exists between many of the parameters (e.g. sea surface salinity with sea surface temperature), has entered the analysis. In practise such correlations could be included on a regional basis to enhance the retrieval accuracy. The information about the regional variability and the parameters' cross correlation could be taken from oceanic and/or atmospheric circulation model results.

8 Miscellaneous

8.1 Acknowledgements

MS is grateful to Beverly de Cuevas and Andrew Coward for help with OCCAM output, and to Graham Quartly for advice on some of the intricacies of MATLAB.

8.2 Appendix

This appendix contains the equations relating L-band brightness temperatures T_b, at h and v-pol, to salinity S and temperature T, used in the simulations in this report. The equations are taken from the papers by Klein & Swift (1977) and Swift & McIntosh (1983). The brightness temperature is a function of the emissivity $e_{h,v}$ at h or v-pol. These in turn are a function of the Fresnel reflection coefficients $R_{h,v}$, which depend on the dielectric constant ε and the incidence angle θ_i. These dependencies are given in the following equations:

a distance of 500 km for a time period of about 10 days will be useful in extending and improving existing climatologies.

It is shown that the errors in salinity obtained from space-borne microwave radiometers may come close to the optimised requirements, and definitely meet the threshold requirements. This means that a microwave radiometer seems capable of providing useful sea surface salinity values, at least for those parts of the ocean where surface water temperature is somewhat above freezing temperature.

Furthermore, it is shown that the relationship between sea surface temperature, brightness temperature and sea surface salinity is only very weakly nonlinear. Consequently, it may be possible to linearise and simplify the relationship between these quantities.

Accurate retrieval of sea surface salinity requires small or no bias in the measurements of brightness temperature. For instance, a bias of ±0.5 K in brightness temperature leads to degradation of the sea surface salinity value. This has implications for the engineering design and subsequent calibration of an L-band passive microwave salinity sensor.

It is also argued that it is not necessary to have simultaneous measurements of sea surface temperature and brightness temperature to retrieve sea surface salinity to useful accuracy. This is not entirely surprising as mesoscale changes in the ocean occur over periods of 10-30 days, typically.

It is important to bear in mind that simplicity rather than completeness has been the guideline for the computations presented in this report. Therefore, model calculations and retrieval simulations should be carried out with a more adequate model of the surface emissivity. In particular, there is a need to further quantify the effects of wind speed, surface roughness, breaking waves and foam on the emissivity, and so on the brightness temperatures, at L-band. This requires first experimental measurements at L-band and then the development of an adequate theoretical description of the effects.

The model calculations have not considered the effect of rain on the attenuation of the radiation leaving the surface to space and the effect of rainfall in modifying the surface roughness. Both will likely influence the radiative transfer in the frequency domain described and have to be considered when developing a retrieval scheme for the surface salinity.

To fully quantify the ability of an L-band passive microwave radiometer to retrieve sea surface salinity to a useful accuracy requires a much more sophisticated simulation study. This would need to include all the geophysical and instrumental sources of error, together with the effects of varying footprint size within the instrument swath, and the actual space-time sampling characteristics of the instrument.

Furthermore, given the sensitivity of the recovery of the sea surface salinity to bias in the measurement of brightness temperature, this implies the need for a careful consideration of how the measured brightness temperatures are to be calibrated to the highest possible accuracy.

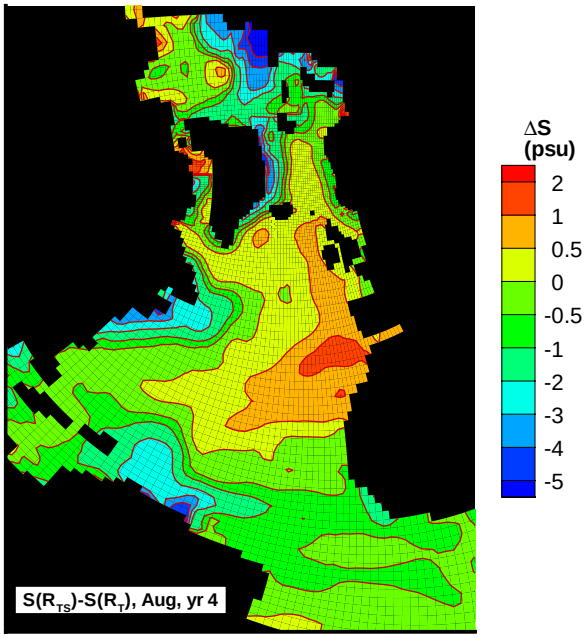

Figure 6-8 Simulated difference in the sea surface salinity field between the model experiment with and without SSS relaxation in March (upper panel) and August (lower panel). Negative numbers indicate a freshening of the simulated SSS field.

7 Summary and Recommendations

The distribution of salt in the global ocean and its temporal and spatial variability are crucial in describing the ocean dynamics, and consequently a quantity that is needed for process studies in general, and climate studies in particular.

The relatively poor distribution of *in situ* salinity measurements over the world oceans can be significantly improved by measurements from space. While satellite measurements of the sea surface and the lower atmosphere have become an integral part of the global observing systems, sea surface salinity has not been monitored from space so far.

In this report, a preliminary assessment of the potential of sea surface salinity observations from space-borne microwave radiometer is carried out. A literature survey indicates that an accuracy of 0.1 psu over a distance of 100 km to 200 km for a time period of about a week is an optimised requirement for description and quantification of many central ocean processes. Given the sparse distribution of *in situ* surface salinity observations, it follows that even a threshold requirement of 1 psu over

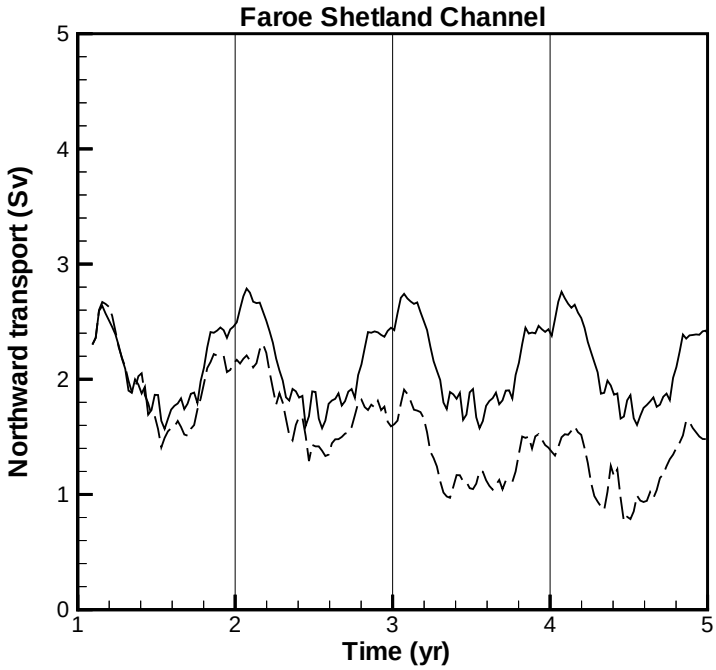

Figure 6-7 Simulated northward (warm and saline) transport in Sv (1 Sv = 10^6 m^3 s^{-1}) of water through the Faeroe-Shetland Channel with both SST and SSS relaxation (solid line), and with only SST relaxation (dashed line).

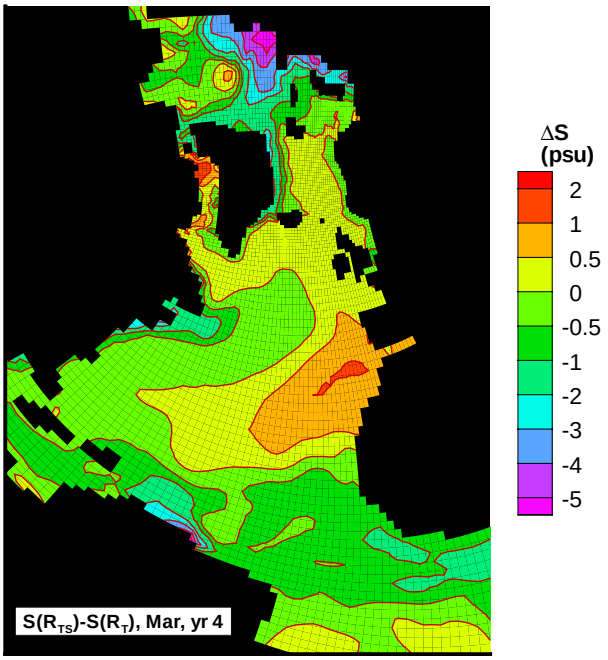

of Drange and Simonsen (1997). The model domains include the Atlantic Ocean from about 20^{o}S and northward, including the Arctic Basin. The horizontal resolution vary from about 200 km in south to about 50 km in the Nordic Seas, and the vertical is discretised in 23 layers of constant density. The model was first spun up for 50 years with monthly mean climatological forcing fields. The long wave, sensible and latent heat fluxes (including the evaporation rate) are explicitly computed based on standard bulk formulas based on the difference in the sea surface and surface atmosphere fields (Drange and Simonsen, 1997), whereas short wave irradiance and precipitation are prescribed climatological fields.

During the spin-up integration, relaxation towards the observed monthly mean Levitus *et al.* (1994) SSS and Levitus and Boyer (1994) SST climatologies were performed. The model reproduces realistic water transports, including the overflow through the Faeroe-Shetland Channel, although the southward transport of surface water through the Greenland Strait is in the lower end of observations. The latter problem is most likely related to insufficient horizontal resolution in the region.

Four experiments were then started, one with continued surface SSS and SST relaxation, one with SSS but no SST relaxation, one with SST but no SSS relaxation, and one without surface relaxation at all. It was found that the model was very insensitive to whether SST was applied or not, indicating that the computed air-sea heat fluxes are reasonably consistent with the observed SST field.

On the contrary, switching off the SSS relaxation changed the general circulation in the North Atlantic in a significant way. This is exemplified in Figure 6-6, which shows a significant reduction in the transport of Atlantic water into the Nordic Seas as the SSS relaxation was removed. The reason for this is that without the SSS relaxation, the surface waters at high latitudes become too fresh (Figure 6-8), leading to a partly shortcut of the thermohaline driving force on the general circulation in the region. The reason for this freshening is not clear, but it indicates erroneous evaporation and/or precipitation rates. This is not surprising; the commonly used evaporation parameterisations are based on rather crude and idealised formulations, and the precipitation field over the ocean is poorly known and constrained.

It should also be noted that changes in the SSS field will lead to changed mixed layer dynamics, including less convective activity during winter time. This again have the potential to change the supply of sub-surface nutrients into the uppermost part of the water column, and thereby affecting the marine biota. Therefore, improved SSS fields may also lead to improved estimates of biological fixation of plant nutrients and carbon. The same conclusion holds for any tracer constituents in the ocean.

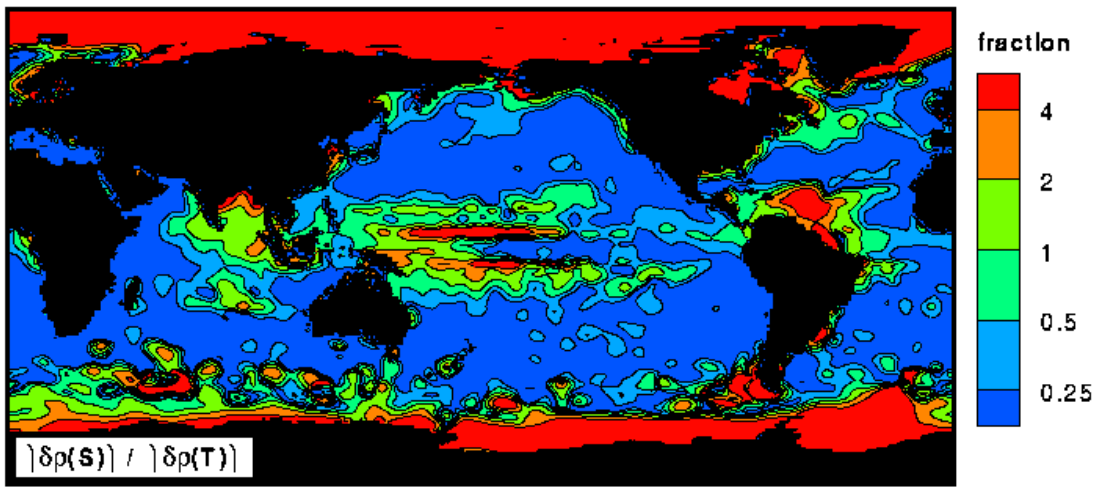

Figure 6-6: The relative magnitude of the annual mean surface water salinity (Levitus et al., 1994) and temperature (Levitus and Boyer, 1994) on sea water density.

Figure 6-6 clearly indicates the importance surface water salinity has on surface water density in polar regions. In addition, it is seen that the Equatorial and Tropical Indian Oceans, the West Tropical Pacific, the Cap Verde Basin, the extension of the Gulf Stream in the North Atlantic, and some coastal regions are all locations where the ocean thermodynamics is specially dependent on the surface water salinity field.

6.2 Simulated SSS Variability and Anomalies in a Basin Scale OGCM

It is well known that the global climate oscillates on a range of time scales. Some of these variations are well documented and fairly well known, others are still being studied. Of particular importance for the North Atlantic region is the approx. decadal oscillations seen in the Greenland ice cores. Several hypothesises have been put forward to describe these oscillations, and most of them include mechanisms related to variations in the flow of saline and warm water from south to north in the Atlantic Basin.

A rather robust result in Atmosphere Ocean Coupled Circulation Models (AOGCM) is that the vertical overturning in the Atlantic Ocean is reduced as the global warming continues. Typical values are 25% to 40% reduction in the overturning over the next century. The reason for the slow down of the northern limb the Global Conveyor Belt circulation is mainly that increased air temperatures lead to increased evaporation at low and intermediate latitudes, and an increased precipitation at high latitudes. This change in the hydrological cycling implies a reduction of the surface water density gradients between low and high latitudes, and decreased deep water formation at high latitudes, and consequently a partly shortcut of the thermohaline circulation.

As far as the AOGCMs represent nature, it is clear that surface salinity is a key component in determining the climate in the North Atlantic sector. Likewise, incorrect surface salinity distributions in OGCMs will lead to an incorrect model climate. A basin scale OGCM has been used to illustrate this statement. The model used is the Miami Isopycnic Coordinate Ocean Model MICOM (Bleck *et al.*, 1992), in the implementation

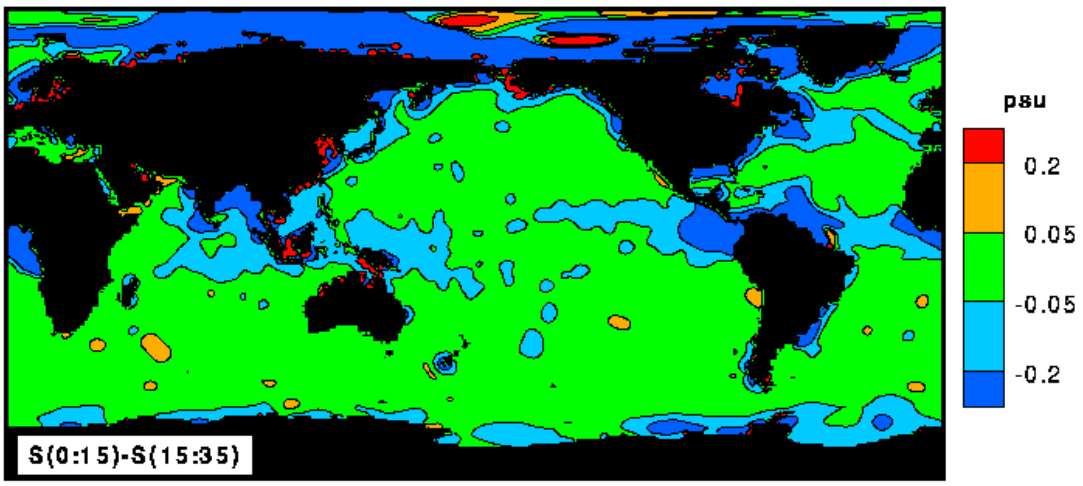

Figure 6-5: The vertical salinity gradients based on the annual mean salinity field of Levitus et al. (1994).

6.1.6 SST and SSS dependency on surface water density

The relative role of surface water temperature and salinity in determing the surface water density can be identified by evaluating the magnitude of the r.h.s. terms of the differential equation (assuming that sea water density is almost constant with respect to pressure for a depth interval of the order 10 m):

Eq. 6-6
$$\left.\frac{\partial \rho\,(S,T)}{\partial z}\right|_{z=20m} = \left.\frac{\partial \rho}{\partial S}\right|_{z=20m}\left(\frac{\partial S}{\partial z}\right) + \left.\frac{\partial \rho}{\partial T}\right|_{z=20m}\left(\frac{\partial T}{\partial z}\right).$$

In the computation of the above equation, the UNESCO Equation of State of Seawater () has been used to assign numerical values to the factors involving ρ, wheras for $\Psi = S$ and T, the change in Ψ with respect to depth has been discretized according to

Eq. 6-7
$$\frac{\partial \Psi(z)}{\partial z} \approx \frac{\Psi(40) - \Psi(0)}{40}.$$

The ratio of the absolute value of the haline and thermal expansion terms are displayed in Figure 6-6 based on the annual mean salinity and temperature fields of Levitus et al. (1994) and Levitus and Boyer (1994), respectively.

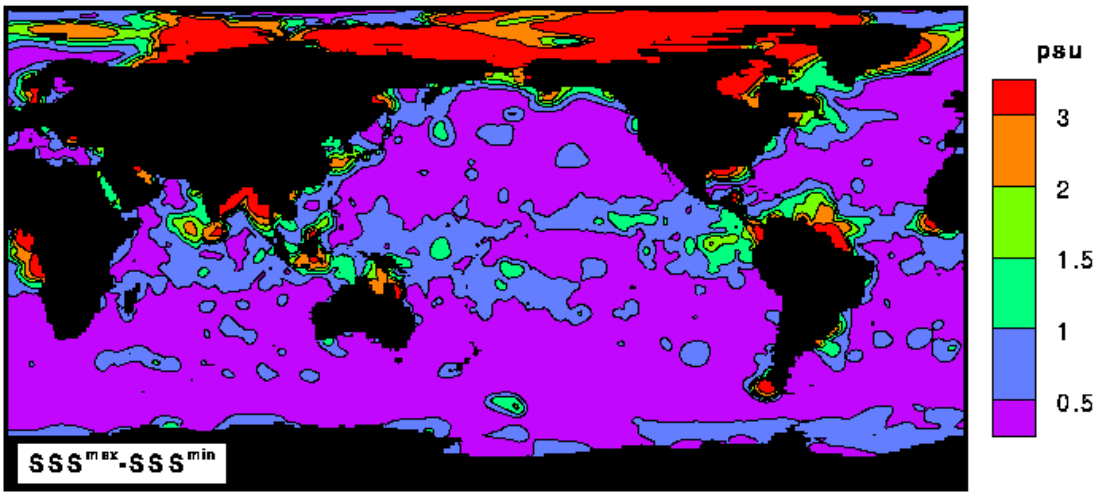

Figure 6-4: Maximum variability in the monthly mean SSS fields according to Levitus et al., 1994.

From Figure 6-4 it follows that the subtropical gyres have a relatively constant SSS throughout the year, that the variability increases in the vicinity of Equator in all Oceans, and that strong variability is found at and near up-welling regions like off West Africa and off Peru, and in regions with large fresh water inputs like Congo, Niger, Amazonas, Putra, Mississippi. In addition, large variability is found along the East Greenland Current and in the Labrador Sea and New Fondland regions, all locations that are heavily affected by the seasonal melting and freezing of sea ice.

6.1.5 Vertical surface salinity gradients

Vertical gradients in salinity over the uppermost part of the water column can be estimated based on the difference in the mean salinity concentrations according to the expressions

$$\Delta S = \left(\overline{S(0{:}15)} - \overline{S(15{:}35)}\right),$$

$$\overline{S(D_1{:}D_2)} = \frac{1}{D_2 - D_1}\int_{D_1}^{D_2} S(z)\,dz.$$

Eq. 6-5

In Figure 6-5, the salinity gradients in the upper ocean are shown based on the annual mean salinity field.

6.1.3 Horizontal gradients in SSS

The maximum horizontal gradients in the monthly mean SSS fields can be quantified by searching for the smallest radial distance *r* from a given location for which the expression

Eq. 6-3
$$\frac{\partial \, \mathrm{SSS}}{\partial r} = 10^{-5} \, \mathrm{psu \ m^{-1}}$$

is met. The obtained distance *r* is shown in Figure 6-3.

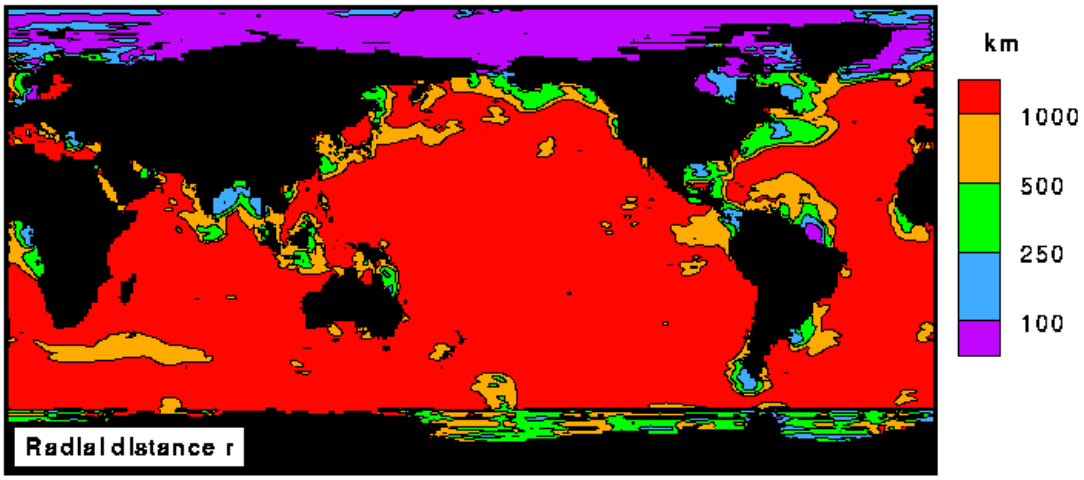

Figure 6-3: Gradients in SSS expressed in terms of the radial distance from Eq. 6-3. Note that r = 100 km indicate that there is a change in the SSS field of 1 psu over a distance of 100 km.

From this figure it follows that coastal regions are generally characterized by quite large gradients in SSS, typically of 1 psu over a distance of 200 to 500 km. The largest gradients are found, as expected, in regions with large fresh water run-off, but also the major part of the Nordic Seas, the Labrador Sea, and the extension of the Gulf Stream are characterized by gradients of about 1 psu over 200 km.

Since the climatological SSS field tends to smooth temporally evolving gradients in the SSS field, and since the horizontal resolution in the Levitus data set is 1-by-1 degree, the displayed radial distance is larger than the actual gradients in the real ocean. For a synoptic SSS field, a dense set of *in situ* salinity observations, or fields from a medium to high resolution OGCM, or – which may be considered as the optimal choice - an OGCM using information from observed SSS, can be used to estimate the real horizontal SSS gradients in the ocean.

6.1.4 Annual variation in SSS

The range of variation in the SSS field over the year has been obtained by subtracting the maximum and minimum monthly mean SSS fields for a given location according to

Eq. 6-4
$$\Delta \mathrm{SSS} = \mathrm{SSS}^{\max} - \mathrm{SSS}^{\min}.$$

The obtained field is shown in Figure 6-4.

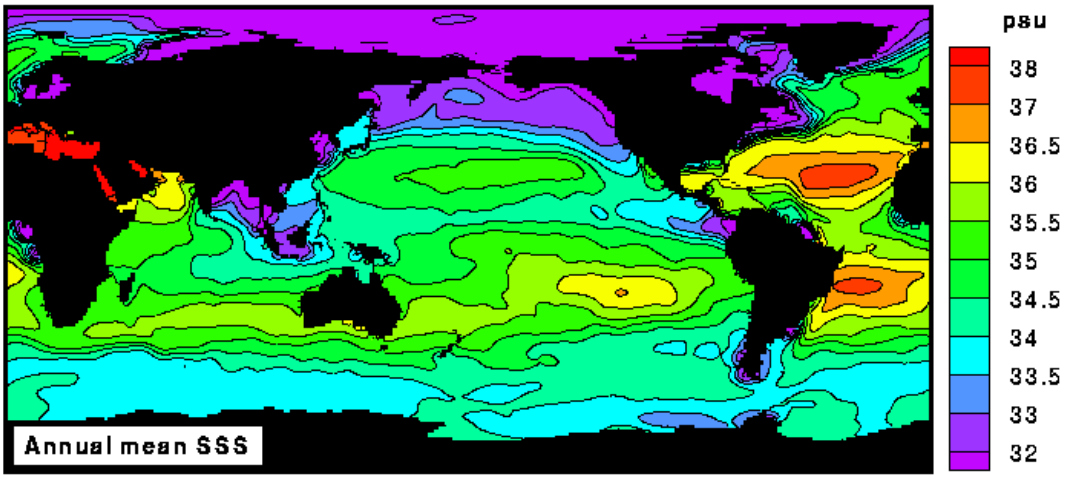

Figure 6-1: Annual mean SSS field (data from Levitus et al., 1994).

The corresponding extent (in km^2) of SSS and SST are shown in Figure 6-2.

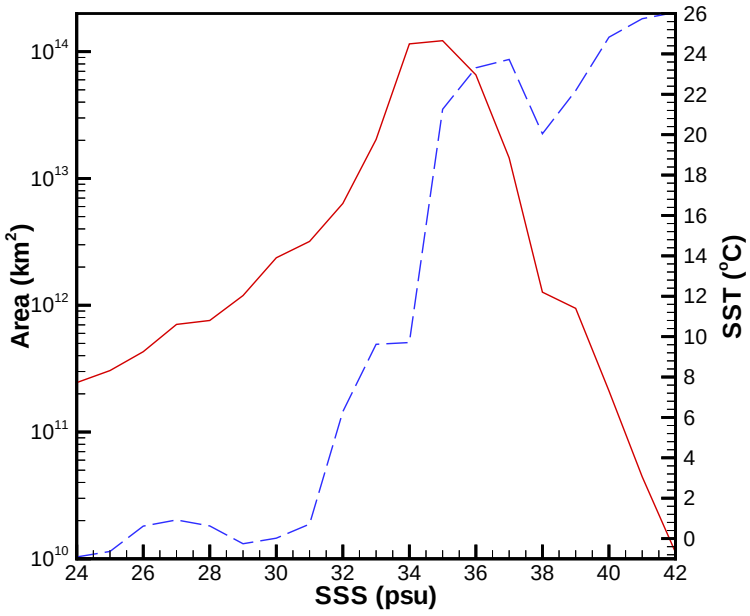

Figure 6-2: Areal distribution of annual mean SSS, and the corresponding mean SST value for the World Oceans (data from Levitus et al., 1994; Levitus and Boyer, 1994).

It follows from Figure 6-1 and Figure 6-2 that the major part of the World Oceans have a salinity of between 34 and 35 psu, that waters with low SSS are more abundant than waters with high SSS and that low (high) SSS are correlated with low (high) SST, and that maximum salinity is found in the Mediterranean Sea, in the Atlantic Subtropical Gyres, and to some extent in the Pacific Subtropical Gyres. Anomalous low SSS regions are found in upwelling regions like off Peru and West Africa, and in regions characterized by large fresh water run-off from rivers like Amazonas, Congo, Mississippi, and the Indian rivers, and in the Baltic.

climatological salinity fields of Levitus *et al.* (1994). These salinity fields are available as monthly, seasonal, and annual mean fields on a 1-by-1 degree latitude-longitude grid (1 degree corresponds to about 111 km at Equator), and on 31 vertical levels with 10 m resolution over the uppermost 50 m of the water column.

The climatological salinity fields have been generated based on a major part of the *in situ* salinity observations over the last 50 years, so the fields are smooth and will therefore tend to underestimate horizontal and vertical gradients in the real ocean. This is particularly true in coastal regions which are often characterized by narrow fresh water current systems. In addition, the SSS fields are by necessity affected by the temporal and spatial resolution of observations. Especially high latitude waters are poorly sampled, so it is hard to make firm conclusions from (very) high latitudes, especially from winter season. Therefore, the results presented below should only be viewed as indicative of the actual spatial and temporal variability in the surface water salinity fields of the World Oceans.

In the following, SSS and *S(z)* denote the sea surface salinity and vertical salinity profile in Practical Salinity Units (psu); z (m) is depth (positive downward); *T(z)* (K) and *p(z)* (Pa) are temperature and pressure, respectively; r (m) is a distance from a given point; and ρ (kg m^{-3}) is sea water density.

6.1.1 Spatial and Temporal Evolution of SSS

The SSS field is governed by the transport equation

Eq. 6-1
$$\frac{\partial SSS}{\partial t} + \nabla \cdot \left(\mathbf{u} SSS \right) = \nabla \cdot \left(K \nabla SSS \right) + f_{SSS} .$$

Here $\mathbf{u}$ (m s^{-1}) is the 3-dimentional velocity field, K (m^2 s^{-1}) is the turbulent diffusion coefficient, and f_{SSS} (s^{-1}) is the rate of change of SSS as result of evaporation, precipitation, formation and melting of sea ice, and river run-off. The above equation expresses that the local SSS field (first term) changes as a result of horizontal and/or vertical advection (second term) or turbulent mixing (third term) of water masses of different SSS value, and of net supply/removal of freshwater.

In case relaxation towards a specified SSS field is performed, Eq. 6-1 is commonly put in the form

Eq. 6-2
$$\frac{\partial SSS}{\partial t} + \nabla \cdot \left(\mathbf{u} SSS \right) = \nabla \cdot \left(K \nabla SSS \right) + f_{SSS} + F\left(SSS_0 - SSS \right),$$

where SSS_0 (-) is the specifield SSS field, and F (s^{-1}) is a tuning parameter that determines how strongly the simulated SSS field should reproduce SSS_0. If the SSS_0 is accurate (or representative), the magnitude of the last term represents the sum of the errors in the other terms, including the SSS forcing term f_{SSS}. Therefore, the magnitude of the relaxation term gives an indication of how well the physics and the SSS forcing are treated.

6.1.2 Annual mean SSS field

The annual mean SSS field according to Levitus *et al.* (1994) is shown in Figure 6-1.

state in a fairly realistic way (Semtner, 1995). In reality, the OGCM suffers from far from perfect initial fields, from atmospheric forcing fields of variable accuracy and variable spatial and temporal resolutions, from parameterizations of the energy and mass transfer that is still not very well known, and from limited computing resources.

Some of the problems related to uncertainties in the atmospheric forcing fields and parameterizations of energy and mass transfer across the air-sea interface can be cured by relaxing the simulated sea surface temperature (SST) and sea surface salinity (SSS) fields towards observed SST and SSS. This approach has been used extensively from the early days of ocean modelling (Haney, 1971), and is commonly used in the ocean modelling community also today. For long time integrations (of the order 1000 years or more) coarse resolution and annual mean observed SST and SSS fields may be sufficient, whereas ocean modelling with focus on seasonal to decadal time scales (as for instance in CLIVAR) requires quite accurate daily to monthly SST and SSS fields with a spatial resolution of the order 100 km.

Inversely, OGCMs that are not forced to closely follow observed SST and SSS fields, or coupled atmosphere-sea ice-ocean climate models that may or may not apply surface flux adjustments, need observed SST and SSS fields for validation of the corresponding simulated fields. It is interesting to note that as the computing resources increase, the need for high quality, high resolution observed ocean state variables increases similarly. This is of coarse a great challenge for the observation community.

Today SST is observed on an approximately weekly basis from space yielding, together with *in situ* SST measurements, fairly accurate and spatially extensive fields of SST. The situation for SSS is completely different as remotely sensed SSS has not been available up to now.

The sea surface temperature and salinity fields are important parts of the thermodynamics of the ocean system. The relative roles of SST and SSS on the ocean thermodynamics, and consequently on the ocean dynamics, depend on location and possibly also the time of the year. In addition, the spatial extent, time scale, and propagation of SST and SSS anomalies in the World Oceans are generally not directly correlated. It is therefore of paramount importance that OGCMs describe *both* SST and SSS in OGCMs in a realistic way.

One important reason for the partly uncoupled behaviour of the SST and SSS fields is that the temporal and spatial scales of interaction between SST and atmosphere (mainly through the air-sea temperature difference) is generally different compared to the corresponding scales of interaction between SSS and atmosphere (through rainfall and evaporation). It also appears that the heat fluxes between air and sea is better known than the evaporation minus precipitation (E-P) fields. This is likely one reason for the statement that in general, SST is more easily simulated than SSS in OGCMs. Any improvement with respect to observed SSS will therefore be of great value for the OGCM community.

6.1 Observed, global monthly mean surface salinity fields

An estimate of the horizontal and vertical gradients, and the seasonal variability of surface water salinity in the World Oceans can be obtained from the global

5.2.5 Conclusions

The simulations presented here based on OCCAM output suffer from the following limitations:

a) The retrieval of S for only one 200^2 km^2 area of the ocean has been performed. Clearly, this may not be fully representative of other parts of the world's ocean.

b) The way the retrievals have been carried out does not capture all the effects that might arise if more realistic sampling were included in the simulation, taking better account of instrument characteristics and satellite orbit.

c) The simulation does not include the effects of wind speed, foam and breaking waves on the emissivity at L-band, as these are not well characterised from measurements.

Despite these limitations, we believe that the results are indicative of the type of accuracy that might be achievable using an L-band passive microwave radiometer to measure *S*. In particular, the fact that using SST values from 2 days after the L-band "measurement" of the brightness temperature makes little difference to the accuracy of the *S* retrieval suggests that it is not necessary to have simultaneous measurements of *T* and T_b to retrieve *S* to useful accuracy. This is not entirely surprising as mesoscale changes in the ocean occur over periods of 10-30 days, typically. Indeed, the Topex altimeter mission orbit repeat cycle of 10 days was chosen so that reasonable sampling of mesoscale phenomena would be possible. So, over a period of 2 days the changes in *S* and *T* should not be a dominant factor in the retrieval of *S*. Additionally, averaging *T* and T_b and then retrieving *S* seems to lead to results with smaller bias. This suggests that it may be best to simply average non-simultaneous measurements of *T* and T_b over the period and area of interest before retrieving *S*.

In terms of meeting the GODAE requirements, the simulations have shown that we can get close to the accuracy of 0.1psu for a 10 day, 200^2km^2 average. This is encouraging, but there are many unaccounted for effects that might increase the error, particularly any bias in the measurement of T_b. This has to be balanced in the potential decrease in the effects of random error if a sensor like MIRAS is used. Its ability to view the same patch of ocean at several different incidence angles as it flies over the area will increase the number of measurements and therefore decrease the error. Investigation of this would require a more complex simulation to be performed. The results also show that a spaceborne L-band passive microwave salinity sensor may contribute useful information to future Levitus-like climatologies of *S*.

6 The Importance of Sea Surface Salinity in Ocean General Circulation Models

The dynamics of the circulation of the World Oceans is governed by energy and mass transfer between the atmosphere, sea ice and ocean systems, fresh water runoff from land, the rotation of the Earth, and the bathymetry of the World Oceans. These components are all included in state-of-the-art ocean general circulation models (OGCMs). In principle, given accurate and consistent initial and atmospheric forcing fields, proper formulation of the energy and mass transfer across the air-sea interface, and sufficient computer resources, the OGCM should be able to describe the ocean

curves almost identical). Retrieving *S* and then averaging seems to lead to a negative bias of O(0.05-0.1psu) (on average the retrieved values of *S* are lower than the "true" values). In contrast, averaging *T* and T_b and then retrieving *S*, seems to lead to little bias. This apparent too from Figs. 5-3 and 5-4 (blue and red curves consistently lower than the green curve).

Table 5-11 OCCAM simulation results for S.

averaging and pol	θ_i**=0°**		θ_i**=50°**	
10 days & 200^2 km^2	**rms error**	**bias**[3]	**rms error**	**Bias**[3]
h-pol	0.1718	-0.0895	0.2384	-0.1328
v-pol	0.1761	-0.0743	0.1394	-0.0614
h-pol (*T* + 2 days)[1]	0.1697	-0.0879	0.2337	-0.0563
v-pol (*T* + 2 days)[1]	0.1817	-0.0684	0.1487	-0.0563
h-pol (T_b, *T* avg)[2]	0.1413	0.0051	0.1886	-0.0011
v-pol (T_b, *T* avg)[2]	0.1584	0.0222	0.1258	0.0231
30 days & 100^2 km^2				
h-pol	0.1541	-0.0563	0.2167	-0.0880
v-pol	0.1189	-0.0678	0.0971	-0.0566

Notes:

1. *T* + 2 days means that the SST values 2 days after the "measurement" of the brightness temperature T_b were used in the retrieval.

2. T_b, T_{avg} means that the brightness temperature and *T* values were averaged over the period and then the *S* values retrieved.

3. Bias is the mean value of the retrieved *S* minus the true *S*. Thus negative values show that the retrieved values are biased low relative to the true values. The rms error and bias are calculated from 36 x 10day values and 12 x 30day values for the 10 days and 200^{2}km^2 and the 30 days and 100^{2}km^2 averages, respectively

One surprising aspect of the results is that the rms errors for the 30 day, 100^2 km^2 averages are lower than for the equivalent case of 10 day, 200^2 km^2 averages. The number of points being averaged are 15 x 4 x 4 = 240 as compared to 5 x 8 x 8 = 320, so the rms error in the latter case might be expected to be smaller. However, the averaging region is larger and therefore the spatial variabilities of *S* and *T* are probably responsible for this result. Plots of the variability of S and T over the 4 x 4 box (not shown) indicate lower degree of variability than that for the 8 x 8 box, as seen in Figs. 5-1 and 5-2.

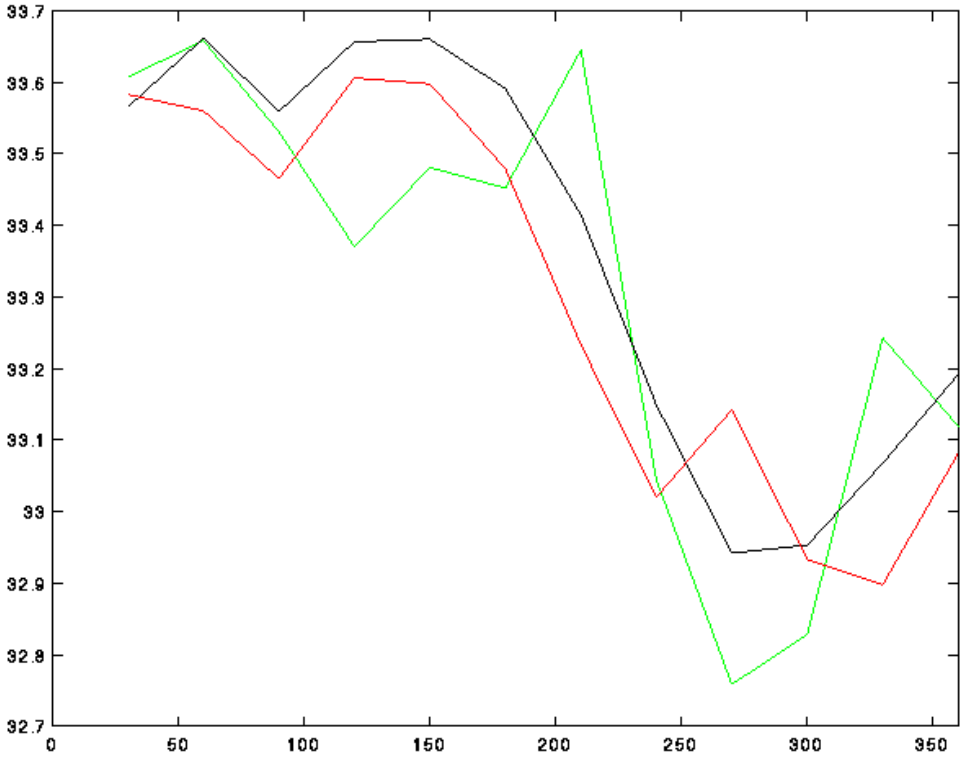

Figure 5-5 Results for salinity retrieval for the 30 day, 100^2 km^2 average at h and v-pol, with θ_i=0°, plotted against day of year. Black curve gives the "true" average value of S *from OCCAM. Green curve is the recovery with noise using h-pol. Red curve is the recovery with noise using v-pol.*

5.2.4 Results and discussion

The results of the simulations are summarised in Table 5-11. There the rms difference and the bias between the retrieved and "true" values of the *S* are given. For the 10 day, 200^2 km^2 average this is calculated from the 36 values obtained over the year. For the 30 day, 100^2 km^2 average this is calculated from the 12 values obtained over the year. Figure 5-3 shows the three types of retrieval (cases A, B and C; see previous section) at h-pol for the 10 day, 200^2 km^2 average, with θ_i=0°, compared with the "true" *S* averaged in the same way. Figure 5-4 shows similar results for v-pol. Finally, Figure 5-5 shows the result at h and v-pol for case A only (see previous section), for the 30 day, 100^2 km^2 average, with θ_i=0°, compared with the "true" *S* averaged in the same way. Results for cases B and C have not been calculated for the 30 day, 100^2 km^2 average, as those for cases A, B and C for the 10 day, 200^2 km^2 average are very similar. Plots of the results for the case θ_i=50° are very similar in form and are not shown. Note that the random noise added to *T* and T_b is identical for cases A, B and C. This was done so as to focus on the effects of the variations in *S* and *T* on the retrieval, rather than those in the random noise.

The results from Table 5-11 show that that *S* can be retrieved with an rms error of ~0.l5 psu, with the smallest rms error being 0.0971 psu and the largest 0.2384 psu. In each case the retrievals are best for v-pol with θ_i=50°, and worst for h-pol at the same incidence angle. For the case where the *T* values 2 days later are used in the retrieval, there appears to be no significant difference from the retrieval using simultaneous "measurements" of *T* and T_b. This is clear seen in Figs. 5-3 and 5-4 (blue and red

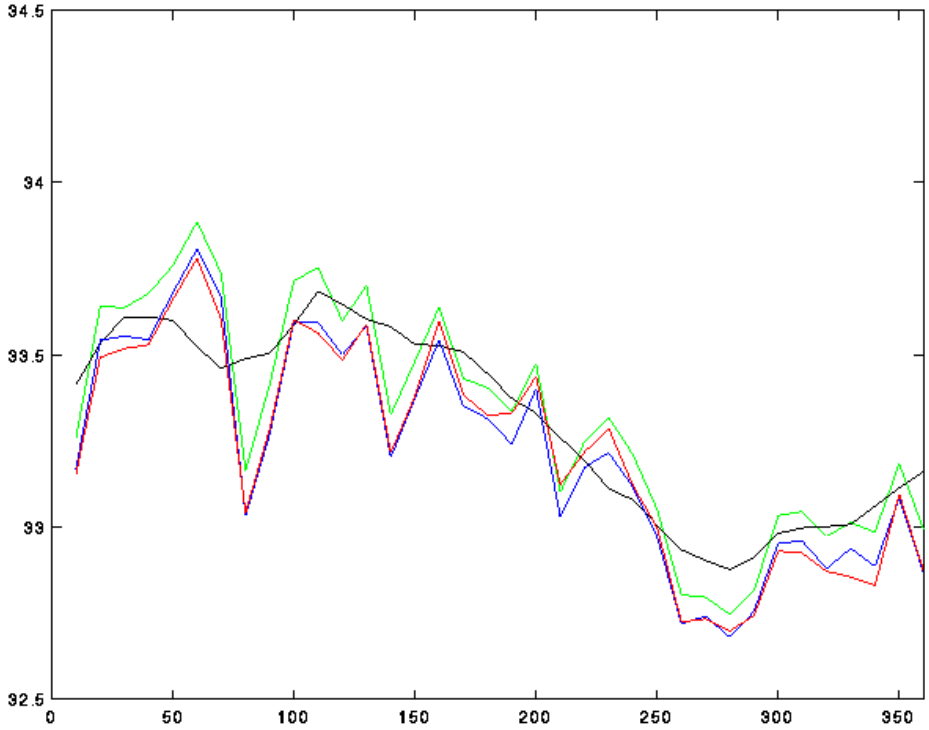

Figure 5-3 Results for salinity retrieval for the 10 day, 200^2 km^2 average at h-pol, with θ_i=0°, plotted against day of year. Black curve gives the "true" average value of S *from OCCAM. Blue curve is the recovery with noise. Red curve is the recovery with noise, but using the* T *value from 2 days after the* T_b *value. Green curve is result from averaging noisy* T *and* T_b*, then retrieving* S*. Blue, red and green curves correspond to cases A, B and C of section 3.*

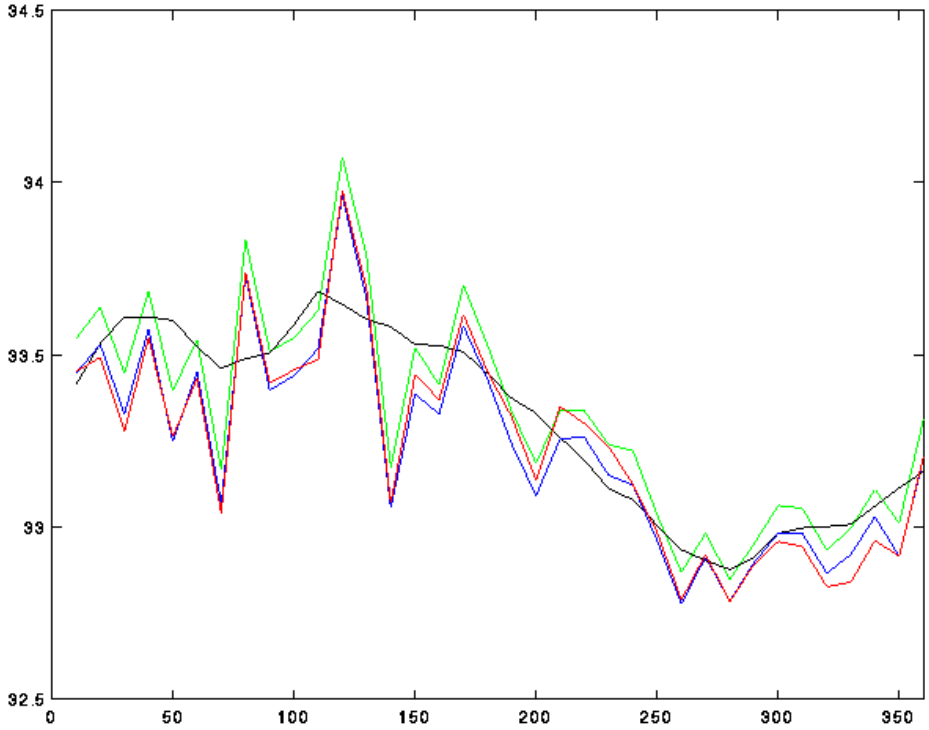

Figure 5-4 Results for salinity retrieval for the 10 day, 200^2 km^2 average at v-pol, with θ_i=0˚, plotted against day of year. Black curve gives the "true" average value of S *from OCCAM. Blue curve is the recovery with noise. Red curve is the recovery with noise, but using the* T *value from 2 days after the* T_b *value. Green curve is result from averaging noisy* T *and* T_b*, then retrieving* S*. Blue, red and green curves correspond to cases A, B and C of section 3.*

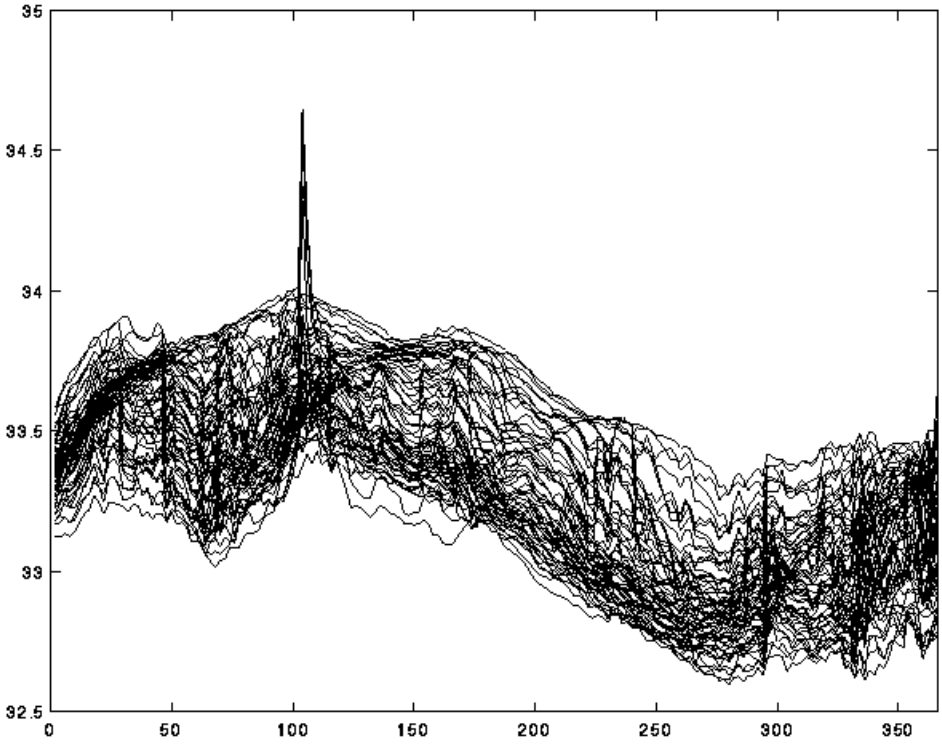

Figure 5-1 The sea surface salinity S *(psu) plotted against day number for the 64 OCCAM grid boxes used in the simulation of SSS retrieval. Note that the OCCAM output exhibits indications of both a seasonal cycle and mesoscale variability.*

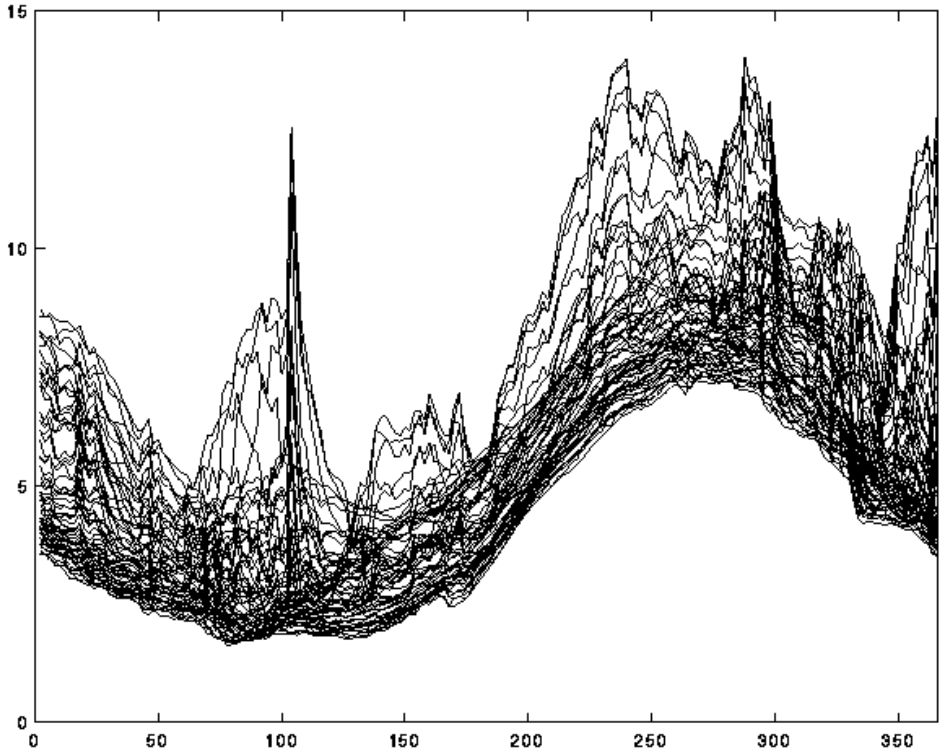

Figure 5-2 The SST T *(°C)plotted against day number for the 64 OCCAM grid boxes used in the simulation of SSS retrieval. Note that the OCCAM output exhibits indications of both a seasonal cycle and mesoscale variability.*

distorted when mapped onto actual latitude and longitude. For the purposes of the simulation we will ignore any effect of this slight distortion.

This particular area of the OCCAM model, in the region of the Grand Banks, has been chosen for the simulation as it is the place where the Labrador Current and the North Atlantic Current meet and interact (Rossby (1996)). Consequently there is considerable variability in both the *S* and the *T*. This variability is illustrated in Figs. 5-1 and 5-2 where the *S* and *T* from OCCAM are plotted for the whole year for all 64 grid boxes in the area. There is evidence of seasonal signals in both *S* and *T*. In addition, there is clearly considerable mesoscale activity, with "spikes", such as that around day 100 probably representing the passage of eddies with different water mass characteristics. This is consistent with it being a region of high eddy kinetic energy (Rossby (1996)). The Levitus climatology (Levitus *et al.* (1994)) also shows that significant variation of the *S* occurs in this area over an annual cycle. Finally, it is also a region where the E-P (evaporation - precipitation, which affects the *S*) varies significantly during the year (Schmitt *et al.* (1989)).

As with the earlier simulations, the 2 day OCCAM values of *S* and *T* for the 64 grid boxes are used to calculate the L-band brightness temperatures T_b at h and v-pol. Normally distributed random noise, with standard deviation of 0.8165 (to be consistent with the earlier simulations) is added to both *T* and T_b. Then three basic retrievals are carried out, at both polarisations and for two incidence angles (θ_i = 0° and 50°). First (case A), for each grid box *S* is retrieved from the noisy *T* and T_b. Second (case B), for each grid box *S* is retrieved from the noisy T_b and the noisy *T* value from 2 days later. This simulates the effect of the non-simultaneous measurement of T_b and *T*. For example, if it were only possible to fly an L-band passive microwave radiometer on the satellite, and *T* had to be obtained from an instrument on another satellite. Third (case C), S is retrieved from the noisy values of *T* and T_b after they have been averaged over the period and area of interest.

The basic averaging is for a 10 day period over the whole 8 x 8 grid, roughly corresponding to 200^2 km^2, along the lines of the GODAE requirement. This assumes that simultaneous measurements are made across the whole area, with a spatial resolution of about 25^2 km^2 and a re-visit time of 2 days. This is not too different from the typical resolution (~30^2 km^2) and re-visit time (~3 days) of proposed L-band radiometer sensor and satellite missions. A secondary averaging is for a 30 day period over the 4 x 4 central part of the grid, which roughly corresponds to 100^2km^2. This is analogous to the monthly 1° x 1° Levitus climatology (Levitus *et al.* (1994)).

Given the results from the earlier, simpler simulations that bias in the "measured" T_b can lead to considerable error in the retrieved *S*, no bias is included in the simulations based on OCCAM output. However, unlike the earlier simulations, the ones carried out here using OCCAM do account for the influence of temporal changes in *S* and *T* over the averaging period in a realistic manner.

5.2.4 and the conclusions that can be drawn from the simulations are given in subsection 5.2.5.

5.2.2 OCCAM: a brief description

OCCAM is a global ocean model run at the Southampton Oceanography Centre, based on the Bryan-Cox-Semtner ocean general circulation model (for details see Webb (1996) and Webb *et al.* (1998)). The model is a primitive equation model, with a free surface. It is of high horizontal resolution, using a 0.25° grid in latitude and longitude. To avoid problems with grid spacing due to convergence of the meridians near the North Pole, the model employs two grids. A standard latitude-longitude grid is used for the Pacific, Indian and South Atlantic Oceans and a rotated grid for the North Atlantic and Arctic Oceans (with "poles" on the Equator in the Indian and Pacific Oceans). The two grids are matched along the equator in the Atlantic. A simple channel model connects the grids through the Bering Strait. The model has 36 vertical levels, ranging in thickness from 20m near the surface to 255m at 5500m depth. The depths were chosen so that the model adequately resolves the mixed layer.

The model was spun up for 8 years (due to limitations on computer time). During the first 4 years the model potential temperature and salinity fields were everywhere relaxed towards the Levitus climatology values (there are some subtleties associated with this process which are discussed by Webb *et al.* (1998), and do not need to be rehearsed here). The surface fluxes of heat and fresh water were calculated so as to relax the surface layer of the model towards Levitus monthly average values (Levitus *et al.* (1994), Levitus & Boyer (1994)). The wind stress forcing was the monthly average ECMWF wind stress climatology of Siefridt & Barnier (1993).

After year 8 there are various continuations of the model run. For the simulations here we use output from one of the so-called AGORA runs (part of a project carried out for the EC). This continued the model integration from day 2922 with atmospheric forcing from ECMWF 6-hourly winds and pressures, starting on 1st January 1992. The results used here are from days 3288 to 3652 of the run, corresponding to the year 1993, in terms of the forcing fields. Sea surface salinity and temperature from OCCAM are available globally every 2 days throughout this period.

5.2.3 Simulation using OCCAM

Clearly a global simulation using OCCAM output is beyond the scope of this report. Therefore, somewhat arbitrarily, we have chosen to concentrate on a "box" of 8 x 8 surface points in the model, for a specific period (one year, days 3288 to 3652). Given the 0.25° resolution of the model, this correspond roughly to a 200^2km^2 area, and allows investigation of the GODAE requirement (10 day, 200^2km^2 averages) and the potential for constructing a Levitus-type climatology (30 day, 100^2km^2 averages). Using a year of OCCAM output covers the effects of seasonal variations in the SSS S and the SST T.

The 8 x 8 box chosen for the simulations is centred at approximately 45°N, 47°W. The co-ordinates of the centres of the corner OCCAM 0.25° grid boxes are (44.13°N, 48.65°W), (44.33°N, 46.23°W), (45.85°N, 48.90°W) and (46.01°N, 46.48°W). Due to the fact that the grid boxes are 0.25° x 0.25° on the rotated grid, they are slightly

5.1.3 Discussion and initial conclusions

What can be concluded from the simulations? First, it appears that the errors in salinity obtained from the averaged values come close to meeting the GODAE optimised requirements (and definitely meet the threshold requirements).[2] The results would be further improved by taking account of the multiple view capability of an instrument like MIRAS. Clearly, as is well known, such measurements will not achieve a WOCE-type accuracy of ±0.002psu (Srokosz (1995); it should be borne in mind that such high accuracy is required for characterising the slow deep flows in the ocean and is not necessarily required for the surface salinity). Nevertheless, the L-band measurements seem capable of providing useful sea surface salinity data, except in those parts of the ocean where the SST values are low (at high latitudes).

Second, recall the fact that uniform errors in T and T_b gave approximately uniform errors in S, and normal errors led to approximately normal errors. Add to this the observation that retrieving S and then averaging gave almost the same result as averaging T and T_b, then retrieving S. Therefore, this suggests the relationship given by Eq. 5-1 is only very weakly nonlinear (this is not at all obvious from the form of the equation; see Klein & Swift (1977) and Swift & McIntosh (1983)). At least this is the case for the range of values of the variables considered in these simulations. This result was unexpected. Consequently, it may be possible to linearise and simplify the relationship.

Third, it is clear that accurate retrieval of S requires there to be little or no bias in the measurements of the brightness temperature T_b. This has implications for the engineering design and subsequent calibration of an L-band passive microwave salinity sensor.

One limitation of the simulation results presented her is that no account has been taken of trends in S or T. It is unlikely that T and S will remain constant over the averaging period, as the ocean is constantly changing. In addition, the observations of T and S will not (in general) be simultaneous, if the measurements are from instruments on different satellites. These problems require a more sophisticated simulation study than that carried out here.

5.2 Retrieval of *S*: simulations using OCCAM

5.2.1 Introduction

Having previously carried out some simple simulations to assess the feasibility of retrieving SSS using an L-band passive microwave radiometer, we now use output from OCCAM (Ocean Circulation and Climate Advanced Model) to perform a somewhat more realistic simulation of SSS retrieval. As for the earlier simulations the dependence of brightness temperature T_b on salinity S and temperature T is taken from the work of Klein & Swift (1977) and Swift & McIntosh (1983). The details of the equations are provided in the appendix.

In the next section a brief description of OCCAM is given. Subsection 5.2.3 describes the simulations that have been carried out. The results are discussed in subsection

[2] Increasing the standard deviations of the errors to 1K, would not affect this conclusion if the errors in S scale as the standard deviations of T and T_b. There would be a factor ~1.22 increase (see footnote 1).

S	S_{avg}	S_{100}	sd S	rms S	T	T_b	T_{100}	T_{b100}	θ_i
33.0	32.798	32.621	4.52	4.51	0.0	91.77	-0.52	91.74	0.0
33.0	33.156	32.998	4.08	4.06	0.0	99.20	-0.36	99.19	25.0
33.0	32.741	32.629	3.06	3.07	0.0	128.74	-0.47	128.78	50.0
33.0	32.781	32.722	2.56	2.56	10.0	92.98	9.40	93.00	0.0
33.0	32.992	32.931	2.53	2.52	10.0	100.57	9.44	100.58	25.0
33.0	32.977	32.945	1.98	1.97	10.0	130.74	9.48	130.76	50.0
33.0	33.235	33.222	1.56	1.57	20.0	93.43	19.60	93.31	0.0
33.0	32.963	32.947	1.53	1.52	20.0	101.19	19.44	101.21	25.0
33.0	32.832	32.821	1.32	1.32	20.0	131.85	19.53	131.97	50.0
33.0	32.898	32.901	0.93	0.93	30.0	92.74	29.53	92.86	0.0
33.0	33.061	33.065	1.08	1.08	30.0	100.58	29.38	100.56	25.0
33.0	33.006	33.004	0.86	0.85	30.0	131.51	29.63	131.48	50.0
35.0	34.931	34.763	4.12	4.10	0.0	91.34	-0.47	91.30	0.0
35.0	34.570	34.476	3.31	3.34	0.0	98.76	-0.36	98.87	25.0
35.0	35.372	35.280	3.20	3.19	0.0	128.21	-0.41	128.10	50.0
35.0	35.045	35.013	2.16	2.15	10.0	92.26	9.54	92.21	0.0
35.0	35.227	35.204	1.94	1.94	10.0	99.84	9.53	99.75	25.0
35.0	34.781	34.748	1.91	1.92	10.0	129.87	9.38	129.94	50.0
35.0	34.846	34.849	1.72	1.72	20.0	92.36	19.50	92.46	0.0
35.0	34.690	34.686	1.16	1.20	20.0	100.07	19.57	100.24	25.0
35.0	34.944	34.937	1.25	1.24	20.0	130.52	19.36	130.56	50.0
35.0	35.140	35.145	1.11	1.12	30.0	91.35	29.40	91.35	0.0
35.0	35.008	35.017	1.33	1.32	30.0	99.15	29.40	99.14	25.0
35.0	35.071	35.070	0.84	0.84	30.0	129.76	29.47	129.69	50.0
37.0	37.021	36.948	3.51	3.50	0.0	90.89	-0.49	90.85	0.0
37.0	36.979	36.886	3.56	3.55	0.0	98.30	-0.53	98.30	25.0
37.0	36.685	36.585	2.91	2.93	0.0	127.63	-0.53	127.72	50.0
37.0	36.751	36.717	2.44	2.45	10.0	91.52	9.50	91.59	0.0
37.0	37.456	37.442	1.78	1.82	10.0	99.07	9.42	98.89	25.0
37.0	36.727	36.696	1.96	1.97	10.0	128.95	9.49	129.08	50.0
37.0	36.804	36.810	1.59	1.60	20.0	91.29	19.58	91.42	0.0
37.0	37.152	37.144	1.59	1.59	20.0	98.95	19.52	98.87	25.0
37.0	37.211	37.202	1.26	1.27	20.0	129.19	19.36	129.06	50.0
37.0	37.096	37.104	1.25	1.25	30.0	89.99	29.51	90.01	0.0
37.0	36.826	36.831	1.06	1.07	30.0	97.70	29.52	97.82	25.0
37.0	37.024	37.025	0.94	0.94	30.0	128.02	29.51	128.00	50.0

Table 5-10 Simulation results for v-pol, no bias in T_b, -0.5K bias in T.

S	S_{avg}	S_{100}	sd S	rms S	T	T_b	T_{100}	T_{b100}	θ_i
33.0	33.004	32.879	3.71	3.69	0.0	91.77	0.53	91.84	0.0
33.0	32.736	32.620	3.48	3.48	0.0	99.36	0.42	99.40	25.0
33.0	33.166	33.062	3.20	3.18	0.0	128.91	0.56	128.89	50.0
33.0	33.529	33.501	2.15	2.19	10.0	92.98	10.52	92.83	0.0
33.0	33.034	33.014	2.08	2.07	10.0	100.69	10.71	100.70	25.0
33.0	32.812	32.770	1.86	1.86	10.0	130.95	10.58	131.02	50.0
33.0	32.638	32.630	1.48	1.52	20.0	93.43	20.52	93.62	0.0
33.0	32.848	32.843	1.40	1.40	20.0	101.18	20.54	101.27	25.0
33.0	32.948	32.942	1.20	1.19	20.0	131.89	20.47	131.93	50.0
33.0	33.071	33.077	1.23	1.22	30.0	92.74	30.52	92.62	0.0
33.0	32.700	32.705	1.05	1.08	30.0	100.46	30.66	100.67	25.0
33.0	32.990	32.988	0.94	0.93	30.0	131.36	30.47	131.40	50.0
35.0	35.229	35.163	2.96	2.95	0.0	91.34	0.58	91.35	0.0
35.0	34.696	34.559	3.76	3.77	0.0	98.89	0.46	98.95	25.0
35.0	34.605	34.482	3.25	3.28	0.0	128.36	0.39	128.46	50.0
35.0	35.178	35.144	2.24	2.23	10.0	92.26	10.56	92.22	0.0
35.0	34.903	34.864	2.42	2.42	10.0	99.91	10.65	99.95	25.0
35.0	34.996	34.973	1.64	1.63	10.0	130.00	10.55	129.99	50.0
35.0	34.967	34.967	1.55	1.54	20.0	92.36	20.52	92.35	0.0
35.0	34.748	34.745	1.37	1.39	20.0	100.03	20.51	100.18	25.0
35.0	34.954	34.953	1.30	1.29	20.0	130.51	20.52	130.54	50.0
35.0	35.020	35.029	1.30	1.29	30.0	91.35	30.57	91.25	0.0
35.0	35.068	35.071	1.12	1.12	30.0	98.96	30.44	98.93	25.0
35.0	34.913	34.918	0.95	0.95	30.0	129.60	30.58	129.66	50.0
37.0	36.841	36.783	3.24	3.23	0.0	90.89	0.54	90.98	0.0
37.0	36.988	36.923	3.44	3.42	0.0	98.40	0.41	98.39	25.0
37.0	37.003	36.893	2.97	2.96	0.0	127.78	0.62	127.81	50.0
37.0	36.894	36.884	2.06	2.05	10.0	91.52	10.48	91.57	0.0
37.0	36.567	36.541	2.35	2.38	10.0	99.11	10.46	99.28	25.0
37.0	37.295	37.279	1.85	1.86	10.0	129.03	10.47	128.89	50.0
37.0	36.847	36.850	1.46	1.46	20.0	91.29	20.57	91.33	0.0
37.0	36.871	36.871	1.42	1.42	20.0	98.88	20.40	98.96	25.0
37.0	36.921	36.917	1.12	1.12	20.0	129.14	20.70	129.18	50.0
37.0	36.785	36.794	1.25	1.26	30.0	89.99	30.40	90.07	0.0
37.0	36.844	36.850	1.04	1.05	30.0	97.54	30.55	97.62	25.0
37.0	36.983	36.983	0.93	0.93	30.0	127.83	30.54	127.84	50.0

Table 5-9 Simulation results for v-pol, no bias in T_b, 0.5K bias in T.

S	S_{avg}	S_{100}	sd S	rms S	T	T_b	T_{100}	T_{b100}	θ_i
33.0	35.442	35.347	3.05	3.83	0.0	91.77	-0.08	91.23	0.0
33.0	35.698	35.591	3.74	4.54	0.0	99.27	-0.05	98.65	25.0
33.0	34.637	34.510	3.34	3.65	0.0	128.81	0.13	128.40	50.0
33.0	34.370	34.351	2.35	2.70	10.0	92.98	10.13	92.50	0.0
33.0	34.213	34.182	2.09	2.40	10.0	100.65	9.94	100.17	25.0
33.0	34.133	34.106	1.92	2.21	10.0	130.83	10.06	130.33	50.0
33.0	33.799	33.792	1.61	1.78	20.0	93.43	20.08	93.00	0.0
33.0	33.668	33.666	1.47	1.61	20.0	101.19	19.98	100.81	25.0
33.0	33.816	33.809	1.24	1.47	20.0	131.88	20.11	131.32	50.0
33.0	33.765	33.769	1.20	1.42	30.0	92.74	30.18	92.18	0.0
33.0	33.696	33.700	1.01	1.23	30.0	100.50	29.79	100.04	25.0
33.0	33.265	33.264	0.96	0.99	30.0	131.47	30.03	131.20	50.0
35.0	37.587	37.532	3.43	4.25	0.0	91.34	-0.03	90.76	0.0
35.0	36.763	36.643	3.64	3.97	0.0	98.82	-0.03	98.40	25.0
35.0	36.618	36.514	3.41	3.71	0.0	128.27	-0.03	127.82	50.0
35.0	36.522	36.494	2.22	2.67	10.0	92.26	10.09	91.70	0.0
35.0	36.148	36.115	2.21	2.46	10.0	99.88	10.00	99.42	25.0
35.0	36.106	36.088	1.85	2.14	10.0	129.92	10.13	129.43	50.0
35.0	36.002	35.994	1.38	1.70	20.0	92.36	20.07	91.82	0.0
35.0	36.064	36.064	1.57	1.89	20.0	100.05	20.05	99.45	25.0
35.0	35.836	35.836	1.10	1.38	20.0	130.52	19.98	129.95	50.0
35.0	35.899	35.906	1.20	1.50	30.0	91.35	29.97	90.74	0.0
35.0	35.876	35.879	1.24	1.52	30.0	99.06	29.96	98.42	25.0
35.0	35.593	35.597	0.96	1.13	30.0	129.68	30.00	129.15	50.0
37.0	39.197	39.089	3.96	4.46	0.0	90.89	0.01	90.39	0.0
37.0	38.597	38.545	3.11	3.46	0.0	98.35	-0.10	97.96	25.0
37.0	38.814	38.769	2.74	3.25	0.0	127.70	0.04	127.20	50.0
37.0	38.077	38.054	2.18	2.41	10.0	91.52	9.97	91.12	0.0
37.0	38.113	38.101	2.05	2.31	10.0	99.09	10.08	98.65	25.0
37.0	37.936	37.912	1.68	1.91	10.0	129.00	9.94	128.55	50.0
37.0	37.720	37.725	1.80	1.93	20.0	91.29	20.03	90.90	0.0
37.0	37.871	37.864	1.43	1.66	20.0	98.92	19.99	98.43	25.0
37.0	37.726	37.720	1.34	1.51	20.0	129.17	20.08	128.67	50.0
37.0	37.723	37.733	1.24	1.44	30.0	89.99	30.10	89.49	0.0
37.0	37.850	37.854	1.08	1.37	30.0	97.59	30.06	96.99	25.0
37.0	37.740	37.745	1.04	1.27	30.0	127.92	30.02	127.29	50.0

Table 5-8 Simulation results for v-pol, no bias in T, -0.5K bias in T_b.

S	S_{avg}	S_{100}	sd S	rms S	T	T_b	T_{100}	T_{b100}	θ_i
33.0	30.296	30.123	4.09	4.99	0.0	91.77	-0.03	92.33	0.0
33.0	30.040	29.858	3.72	4.86	0.0	99.27	-0.06	99.92	25.0
33.0	31.152	31.018	3.40	3.92	0.0	128.80	0.21	129.35	50.0
33.0	31.642	31.581	2.42	2.79	10.0	92.98	9.81	93.45	0.0
33.0	31.888	31.859	2.06	2.34	10.0	100.62	10.07	101.07	25.0
33.0	31.740	31.695	2.04	2.41	10.0	130.85	9.94	131.39	50.0
33.0	32.345	32.332	1.57	1.70	20.0	93.43	19.97	93.78	0.0
33.0	32.122	32.117	1.42	1.67	20.0	101.19	20.09	101.69	25.0
33.0	32.430	32.415	1.24	1.36	20.0	131.88	19.98	132.26	50.0
33.0	32.262	32.265	1.15	1.36	30.0	92.74	29.76	93.28	0.0
33.0	32.203	32.206	1.14	1.38	30.0	100.55	30.01	101.12	25.0
33.0	32.518	32.520	1.00	1.10	30.0	131.44	30.06	131.87	50.0
35.0	32.473	32.327	4.07	4.86	0.0	91.34	0.04	91.89	0.0
35.0	32.525	32.361	4.02	4.79	0.0	98.82	0.00	99.38	25.0
35.0	33.117	33.038	2.89	3.48	0.0	128.27	0.03	128.79	50.0
35.0	33.372	33.341	2.35	2.87	10.0	92.26	9.81	92.83	0.0
35.0	33.174	33.138	2.25	2.91	10.0	99.86	9.94	100.57	25.0
35.0	34.055	34.028	1.67	1.93	10.0	129.92	10.05	130.37	50.0
35.0	33.788	33.785	1.50	1.93	20.0	92.36	19.96	93.01	0.0
35.0	34.344	34.344	1.51	1.64	20.0	100.05	19.86	100.43	25.0
35.0	34.282	34.274	1.19	1.39	20.0	130.52	20.16	131.01	50.0
35.0	34.192	34.199	1.21	1.44	30.0	91.35	29.97	91.91	0.0
35.0	34.326	34.326	1.02	1.22	30.0	99.06	30.12	99.53	25.0
35.0	34.464	34.463	0.87	1.02	30.0	129.65	29.86	130.16	50.0
37.0	34.572	34.445	4.18	4.88	0.0	90.89	0.05	91.44	0.0
37.0	34.882	34.762	3.64	4.26	0.0	98.35	0.00	98.85	25.0
37.0	35.218	35.118	3.02	3.55	0.0	127.71	-0.06	128.20	50.0
37.0	35.732	35.703	2.38	2.70	10.0	91.52	9.93	91.98	0.0
37.0	35.875	35.847	2.06	2.35	10.0	99.09	9.96	99.53	25.0
37.0	35.994	35.975	1.91	2.16	10.0	128.99	10.07	129.47	50.0
37.0	36.202	36.205	1.54	1.72	20.0	91.29	19.89	91.72	0.0
37.0	35.885	35.884	1.56	1.91	20.0	98.93	19.95	99.55	25.0
37.0	36.440	36.437	1.22	1.34	20.0	129.17	20.03	129.54	50.0
37.0	36.235	36.240	1.14	1.37	30.0	89.99	30.00	90.51	0.0
37.0	36.137	36.142	1.17	1.44	30.0	97.61	29.96	98.24	25.0
37.0	36.313	36.317	1.03	1.23	30.0	127.94	29.91	128.54	50.0

Table 5-7 Simulation results for v-pol, no bias in T, 0.5K bias in T_b.

S	S_{avg}	S_{100}	sd S	rms S	T	T_b	T_{100}	T_{b100}	θ_i
33.0	32.662	32.492	4.17	4.18	0.0	91.77	-0.39	91.79	0.0
33.0	32.632	32.392	5.11	5.12	0.0	84.65	-0.54	84.70	25.0
33.0	32.894	32.667	5.09	5.08	0.0	63.20	-0.62	63.21	50.0
33.0	33.314	33.281	2.35	2.35	10.0	92.98	9.46	92.82	0.0
33.0	32.987	32.940	2.61	2.60	10.0	85.73	9.58	85.74	25.0
33.0	33.169	33.094	3.42	3.40	10.0	63.94	9.49	63.89	50.0
33.0	33.541	33.538	1.62	1.70	20.0	93.43	19.44	93.15	0.0
33.0	32.889	32.884	1.52	1.52	20.0	86.13	19.45	86.19	25.0
33.0	32.968	32.958	1.95	1.94	20.0	64.12	19.49	64.14	50.0
33.0	33.033	33.037	1.21	1.20	30.0	92.74	29.52	92.77	0.0
33.0	33.017	33.024	1.42	1.42	30.0	85.48	29.44	85.48	25.0
33.0	32.991	32.999	1.66	1.65	30.0	63.50	29.61	63.49	50.0
35.0	34.779	34.646	3.83	3.82	0.0	91.34	-0.55	91.32	0.0
35.0	36.095	35.980	3.71	3.82	0.0	84.23	-0.37	84.03	25.0
35.0	34.951	34.743	5.24	5.22	0.0	62.90	-0.40	62.91	50.0
35.0	34.981	34.940	2.37	2.36	10.0	92.26	9.50	92.23	0.0
35.0	34.941	34.895	2.51	2.49	10.0	85.06	9.49	85.08	25.0
35.0	34.665	34.623	3.10	3.11	10.0	63.41	9.52	63.50	50.0
35.0	34.777	34.774	1.48	1.49	20.0	92.36	19.62	92.49	0.0
35.0	34.870	34.872	1.53	1.52	20.0	85.14	19.34	85.21	25.0
35.0	35.473	35.477	2.06	2.10	20.0	63.35	19.62	63.16	50.0
35.0	35.332	35.336	1.08	1.13	30.0	91.35	29.46	91.21	0.0
35.0	35.020	35.028	1.26	1.26	30.0	84.20	29.46	84.19	25.0
35.0	34.946	34.961	1.86	1.85	30.0	62.49	29.43	62.52	50.0
37.0	36.932	36.837	3.16	3.15	0.0	90.89	-0.47	90.87	0.0
37.0	37.343	37.179	4.10	4.08	0.0	83.83	-0.53	83.76	25.0
37.0	36.603	36.464	4.63	4.64	0.0	62.57	-0.37	62.64	50.0
37.0	36.946	36.922	2.21	2.21	10.0	91.52	9.49	91.52	0.0
37.0	37.104	37.080	2.56	2.55	10.0	84.38	9.49	84.35	25.0
37.0	37.031	37.002	3.00	2.98	10.0	62.87	9.53	62.86	50.0
37.0	36.930	36.932	1.55	1.54	20.0	91.29	19.55	91.36	0.0
37.0	37.173	37.175	1.69	1.69	20.0	84.15	19.55	84.07	25.0
37.0	37.028	37.031	2.34	2.33	20.0	62.57	19.78	62.54	50.0
37.0	37.113	37.121	1.30	1.30	30.0	89.99	29.43	90.02	0.0
37.0	36.732	36.737	1.18	1.20	30.0	82.94	29.55	83.09	25.0
37.0	37.288	37.298	1.57	1.59	30.0	61.49	29.54	61.36	50.0

Table 5-6 Simulation results for h-pol, no bias in T_b, -0.5K bias in T.

S	S_{avg}	S_{100}	sd S	rms S	T	T_b	T_{100}	T_{b100}	θ_i
33.0	33.367	33.229	4.10	4.08	0.0	91.77	0.47	91.75	0.0
33.0	32.993	32.762	4.28	4.27	0.0	84.75	0.48	84.76	25.0
33.0	32.894	32.619	5.42	5.41	0.0	63.29	0.59	63.31	50.0
33.0	33.365	33.338	2.08	2.09	10.0	92.98	10.55	92.90	0.0
33.0	32.840	32.797	2.29	2.29	10.0	85.81	10.62	85.88	25.0
33.0	33.151	33.090	3.05	3.03	10.0	63.99	10.41	63.94	50.0
33.0	33.257	33.237	1.28	1.29	20.0	93.43	20.43	93.28	0.0
33.0	32.932	32.925	1.63	1.62	20.0	86.12	20.62	86.15	25.0
33.0	33.162	33.157	1.89	1.89	20.0	64.10	20.60	64.03	50.0
33.0	32.932	32.936	1.16	1.15	30.0	92.74	30.79	92.68	0.0
33.0	32.941	32.943	1.11	1.10	30.0	85.32	30.60	85.38	25.0
33.0	33.141	33.149	1.38	1.38	30.0	63.37	30.40	63.32	50.0
35.0	35.701	35.588	3.44	3.48	0.0	91.34	0.54	91.24	0.0
35.0	35.520	35.436	3.78	3.78	0.0	84.34	0.68	84.24	25.0
35.0	35.025	34.856	4.66	4.63	0.0	62.97	0.61	62.96	50.0
35.0	35.179	35.151	2.42	2.41	10.0	92.26	10.50	92.22	0.0
35.0	35.040	35.009	2.45	2.44	10.0	85.11	10.44	85.09	25.0
35.0	35.218	35.185	2.72	2.71	10.0	63.43	10.46	63.37	50.0
35.0	35.009	35.004	1.50	1.49	20.0	92.36	20.53	92.33	0.0
35.0	35.137	35.131	1.35	1.34	20.0	85.09	20.45	85.03	25.0
35.0	34.786	34.792	2.33	2.32	20.0	63.30	20.43	63.38	50.0
35.0	35.209	35.213	1.16	1.17	30.0	91.35	30.50	91.13	0.0
35.0	35.139	35.147	1.32	1.32	30.0	84.05	30.31	83.98	25.0
35.0	35.212	35.220	1.40	1.41	30.0	62.38	30.27	62.28	50.0
37.0	37.034	36.950	3.29	3.27	0.0	90.89	0.55	90.93	0.0
37.0	36.844	36.744	4.12	4.11	0.0	83.91	0.44	83.93	25.0
37.0	36.882	36.720	4.39	4.38	0.0	62.61	0.48	62.63	50.0
37.0	36.899	36.875	2.11	2.11	10.0	91.52	10.55	91.57	0.0
37.0	37.112	37.075	2.47	2.46	10.0	84.40	10.52	84.36	25.0
37.0	37.077	37.060	2.79	2.77	10.0	62.87	10.50	62.85	50.0
37.0	37.047	37.047	1.58	1.57	20.0	91.29	20.58	91.22	0.0
37.0	37.441	37.445	1.73	1.78	20.0	84.07	20.42	83.86	25.0
37.0	36.931	36.933	2.00	1.99	20.0	62.50	20.51	62.52	50.0
37.0	37.026	37.037	1.36	1.35	30.0	89.99	30.38	89.91	0.0
37.0	36.895	36.905	1.38	1.38	30.0	82.78	30.43	82.84	25.0
37.0	37.127	37.149	1.75	1.75	30.0	61.37	30.65	61.27	50.0

Table 5-5 Simulation results for h-pol, no bias in T_b, 0.5K bias in T.

S	S_{avg}	S_{100}	sd S	rms S	T	T_b	T_{100}	T_{b100}	θ_i
33.0	34.838	34.710	3.77	4.12	0.0	91.77	0.00	91.37	0.0
33.0	34.998	34.883	3.86	4.27	0.0	84.69	-0.13	84.27	25.0
33.0	35.150	35.003	4.80	5.18	0.0	63.24	0.13	62.91	50.0
33.0	34.005	33.980	2.27	2.46	10.0	92.98	9.98	92.62	0.0
33.0	34.196	34.162	2.31	2.58	10.0	85.77	9.96	85.36	25.0
33.0	35.041	35.007	3.13	3.70	10.0	63.96	10.09	63.41	50.0
33.0	33.694	33.685	1.55	1.68	20.0	93.43	19.87	93.06	0.0
33.0	33.912	33.906	1.40	1.66	20.0	86.13	19.89	85.67	25.0
33.0	33.965	33.965	2.25	2.44	20.0	64.12	19.98	63.73	50.0
33.0	33.803	33.806	1.14	1.39	30.0	92.74	29.96	92.18	0.0
33.0	33.584	33.593	1.30	1.42	30.0	85.42	30.12	85.02	25.0
33.0	34.133	34.148	1.69	2.03	30.0	63.43	29.98	62.86	50.0
35.0	37.237	37.154	3.61	4.19	0.0	91.34	-0.08	90.83	0.0
35.0	37.134	36.945	4.37	4.76	0.0	84.28	-0.06	83.83	25.0
35.0	38.221	38.070	5.12	5.95	0.0	62.92	-0.08	62.38	50.0
35.0	36.070	36.064	2.18	2.42	10.0	92.26	10.04	91.86	0.0
35.0	36.823	36.797	2.35	2.95	10.0	85.09	9.97	84.45	25.0
35.0	37.271	37.231	2.86	3.61	10.0	63.42	9.95	62.80	50.0
35.0	36.124	36.124	1.50	1.87	20.0	92.36	19.96	91.76	0.0
35.0	36.157	36.152	1.74	2.08	20.0	85.12	19.89	84.55	25.0
35.0	36.230	36.234	1.98	2.33	20.0	63.33	20.11	62.83	50.0
35.0	35.643	35.648	1.25	1.40	30.0	91.35	30.05	90.90	0.0
35.0	35.787	35.791	1.16	1.40	30.0	84.11	30.16	83.59	25.0
35.0	36.101	36.113	1.71	2.03	30.0	62.40	29.96	61.88	50.0
37.0	38.986	38.906	3.45	3.93	0.0	90.89	-0.01	90.44	0.0
37.0	38.897	38.798	3.67	4.07	0.0	83.87	-0.08	83.45	25.0
37.0	40.000	39.916	4.66	5.48	0.0	62.59	0.15	62.07	50.0
37.0	38.197	38.175	2.42	2.68	10.0	91.52	10.14	91.07	0.0
37.0	38.482	38.470	2.17	2.61	10.0	84.39	10.10	83.87	25.0
37.0	38.872	38.837	3.16	3.64	10.0	62.87	10.01	62.36	50.0
37.0	38.063	38.068	1.85	2.13	20.0	91.29	19.96	90.73	0.0
37.0	37.902	37.913	1.85	2.06	20.0	84.12	20.03	83.66	25.0
37.0	38.557	38.560	2.09	2.60	20.0	62.53	19.93	61.93	50.0
37.0	37.792	37.800	1.25	1.48	30.0	89.99	29.96	89.47	0.0
37.0	37.948	37.954	1.16	1.50	30.0	82.85	30.08	82.24	25.0
37.0	38.466	38.483	1.73	2.27	30.0	61.42	29.93	60.73	50.0

Table 5-4 Simulation results for h-pol, no bias in T, -0.5K bias in T_b.

S	S_{avg}	S_{100}	sd S	rms S	T	T_b	T_{100}	T_{b100}	θ_i
33.0	30.408	30.275	3.52	4.44	0.0	91.77	0.04	92.32	0.0
33.0	30.000	29.612	5.06	6.07	0.0	84.70	-0.03	85.29	25.0
33.0	31.111	30.902	4.84	5.26	0.0	63.25	-0.08	63.54	50.0
33.0	31.301	31.255	2.51	3.04	10.0	92.98	10.12	93.60	0.0
33.0	31.744	31.688	2.31	2.65	10.0	85.78	9.88	86.18	25.0
33.0	31.210	31.131	3.25	3.73	10.0	63.96	10.01	64.44	50.0
33.0	32.618	32.614	1.57	1.61	20.0	93.43	19.97	93.63	0.0
33.0	32.049	32.048	1.65	1.90	20.0	86.13	20.00	86.60	25.0
33.0	31.339	31.331	2.07	2.65	20.0	64.11	20.07	64.77	50.0
33.0	32.258	32.256	1.00	1.24	30.0	92.74	29.99	93.26	0.0
33.0	32.325	32.326	1.20	1.37	30.0	85.42	30.10	85.85	25.0
33.0	32.090	32.097	1.36	1.63	30.0	63.43	30.12	63.90	50.0
35.0	32.912	32.727	4.16	4.72	0.0	91.34	0.01	91.79	0.0
35.0	32.862	32.737	3.73	4.34	0.0	84.29	-0.11	84.71	25.0
35.0	32.245	31.930	5.46	6.24	0.0	62.92	-0.02	63.37	50.0
35.0	33.736	33.700	2.04	2.41	10.0	92.26	10.01	92.72	0.0
35.0	33.345	33.319	2.25	2.80	10.0	85.09	9.98	85.65	25.0
35.0	32.911	32.861	3.49	4.08	10.0	63.42	9.96	63.98	50.0
35.0	33.878	33.884	1.55	1.91	20.0	92.36	20.01	92.96	0.0
35.0	33.708	33.704	1.67	2.11	20.0	85.12	20.14	85.77	25.0
35.0	33.804	33.809	2.35	2.63	20.0	63.31	19.99	63.79	50.0
35.0	34.295	34.298	1.11	1.31	30.0	91.35	29.99	91.84	0.0
35.0	34.059	34.058	1.19	1.51	30.0	84.12	30.00	84.73	25.0
35.0	33.821	33.835	1.68	2.04	30.0	62.42	30.08	63.01	50.0
37.0	34.262	34.124	3.77	4.72	0.0	90.89	0.02	91.50	0.0
37.0	34.333	34.186	4.26	5.08	0.0	83.87	0.02	84.43	25.0
37.0	34.702	34.445	5.37	5.92	0.0	62.59	-0.04	62.97	50.0
37.0	35.764	35.741	2.39	2.69	10.0	91.52	9.96	91.97	0.0
37.0	35.631	35.603	2.22	2.61	10.0	84.39	9.95	84.87	25.0
37.0	35.327	35.288	2.89	3.35	10.0	62.87	10.10	63.33	50.0
37.0	35.727	35.723	1.74	2.15	20.0	91.29	20.04	91.96	0.0
37.0	35.782	35.779	1.40	1.85	20.0	84.11	19.85	84.74	25.0
37.0	35.596	35.602	2.23	2.62	20.0	62.55	20.12	63.08	50.0
37.0	36.428	36.434	1.18	1.30	30.0	89.99	29.97	90.38	0.0
37.0	36.253	36.264	1.41	1.59	30.0	82.85	30.09	83.30	25.0
37.0	36.101	36.125	1.94	2.12	30.0	61.42	30.06	61.87	50.0

Table 5-3 Simulation results for h-pol, no bias in T, 0.5K bias in T_b.

S	S_{avg}	S_{100}	sd S	rms S	T	T_b	T_{100}	T_{b100}	θ_i
33.0	33.087	32.898	4.10	4.08	0.0	91.77	-0.09	91.74	0.0
33.0	33.100	33.008	3.21	3.20	0.0	99.26	-0.06	99.25	25.0
33.0	33.123	33.004	3.29	3.27	0.0	128.80	0.13	128.81	50.0
33.0	32.845	32.801	2.50	2.49	10.0	92.98	10.07	93.05	0.0
33.0	32.976	32.922	2.30	2.29	10.0	100.65	9.99	100.65	25.0
33.0	32.835	32.793	1.68	1.69	10.0	130.84	9.84	130.89	50.0
33.0	33.175	33.168	1.57	1.58	20.0	93.43	20.05	93.33	0.0
33.0	32.909	32.905	1.40	1.40	20.0	101.19	20.09	101.24	25.0
33.0	33.012	33.004	1.17	1.17	20.0	131.88	19.90	131.86	50.0
33.0	32.848	32.855	1.20	1.20	30.0	92.74	30.15	92.82	0.0
33.0	33.069	33.074	1.18	1.17	30.0	100.51	30.03	100.47	25.0
33.0	32.953	32.952	0.81	0.81	30.0	131.44	29.94	131.49	50.0
35.0	35.795	35.722	3.20	3.26	0.0	91.34	-0.05	91.16	0.0
35.0	34.995	34.871	3.84	3.82	0.0	98.81	0.05	98.83	25.0
35.0	34.760	34.678	2.94	2.94	0.0	128.28	0.01	128.34	50.0
35.0	34.946	34.898	2.27	2.26	10.0	92.26	10.03	92.28	0.0
35.0	34.992	34.956	2.06	2.05	10.0	99.87	10.12	99.88	25.0
35.0	34.752	34.712	2.01	2.02	10.0	129.94	10.00	130.04	50.0
35.0	34.769	34.769	1.50	1.51	20.0	92.36	19.93	92.48	0.0
35.0	35.088	35.080	1.47	1.46	20.0	100.06	19.96	100.00	25.0
35.0	34.934	34.920	1.33	1.32	20.0	130.52	20.14	130.56	50.0
35.0	34.862	34.866	1.06	1.06	30.0	91.35	30.05	91.44	0.0
35.0	35.196	35.198	0.95	0.96	30.0	99.05	30.14	98.89	25.0
35.0	35.053	35.056	1.01	1.00	30.0	129.65	29.96	129.63	50.0
37.0	37.499	37.455	2.91	2.93	0.0	90.89	0.00	90.78	0.0
37.0	37.444	37.356	3.46	3.46	0.0	98.35	0.05	98.25	25.0
37.0	36.399	36.328	2.91	2.97	0.0	127.72	-0.06	127.87	50.0
37.0	36.605	36.585	2.28	2.30	10.0	91.52	10.02	91.67	0.0
37.0	36.934	36.905	1.95	1.94	10.0	99.09	9.95	99.11	25.0
37.0	37.314	37.294	1.75	1.76	10.0	128.99	10.12	128.86	50.0
37.0	36.905	36.908	1.63	1.63	20.0	91.29	19.98	91.34	0.0
37.0	36.954	36.957	1.42	1.41	20.0	98.92	19.93	98.95	25.0
37.0	36.843	36.841	1.42	1.43	20.0	129.17	19.80	129.28	50.0
37.0	37.021	37.027	1.21	1.20	30.0	89.99	30.20	89.94	0.0
37.0	37.171	37.174	1.13	1.14	30.0	97.57	30.04	97.48	25.0
37.0	36.948	36.950	0.84	0.84	30.0	127.92	29.98	127.98	50.0

Table 5-2 Simulation results for v-pol, no bias in T or T_b.

S	S_{avg}	S_{100}	sd S	rms S	T	T_b	T_{100}	T_{b100}	θ_i
33.0	32.949	32.827	3.47	3.45	0.0	91.77	-0.07	91.77	0.0
33.0	32.830	32.671	4.03	4.02	0.0	84.69	-0.10	84.72	25.0
33.0	33.632	33.410	5.40	5.39	0.0	63.24	-0.08	63.14	50.0
33.0	32.996	32.961	1.92	1.91	10.0	92.98	10.00	92.98	0.0
33.0	32.699	32.655	2.17	2.19	10.0	85.77	9.87	85.86	25.0
33.0	33.113	33.056	3.38	3.37	10.0	63.96	9.95	63.93	50.0
33.0	32.975	32.973	1.49	1.48	20.0	93.43	20.05	93.44	0.0
33.0	32.571	32.564	1.58	1.63	20.0	86.13	20.04	86.34	25.0
33.0	32.914	32.906	2.18	2.17	20.0	64.11	20.06	64.14	50.0
33.0	32.998	33.002	1.18	1.17	30.0	92.74	30.04	92.73	0.0
33.0	32.892	32.900	1.32	1.31	30.0	85.42	30.04	85.49	25.0
33.0	32.874	32.885	1.72	1.72	30.0	63.44	30.07	63.50	50.0
35.0	34.664	34.557	3.66	3.67	0.0	91.34	0.00	91.41	0.0
35.0	35.392	35.307	3.41	3.41	0.0	84.29	0.00	84.21	25.0
35.0	35.233	35.034	5.16	5.13	0.0	62.93	-0.05	62.88	50.0
35.0	35.070	35.045	2.33	2.32	10.0	92.26	9.96	92.23	0.0
35.0	34.995	34.975	2.53	2.52	10.0	85.08	10.10	85.09	25.0
35.0	34.716	34.656	3.57	3.57	10.0	63.42	9.90	63.50	50.0
35.0	34.948	34.943	1.40	1.39	20.0	92.36	20.01	92.38	0.0
35.0	34.777	34.774	1.68	1.69	20.0	85.12	20.05	85.23	25.0
35.0	35.196	35.193	2.22	2.21	20.0	63.32	19.98	63.24	50.0
35.0	34.915	34.926	1.36	1.36	30.0	91.35	29.93	91.42	0.0
35.0	34.975	34.980	1.26	1.26	30.0	84.13	30.05	84.13	25.0
35.0	35.091	35.104	1.53	1.52	30.0	62.42	30.00	62.38	50.0
37.0	36.512	36.372	4.44	4.46	0.0	90.89	-0.05	91.00	0.0
37.0	36.707	36.584	3.88	3.88	0.0	83.86	0.00	83.93	25.0
37.0	37.249	37.123	5.11	5.08	0.0	62.59	-0.11	62.55	50.0
37.0	36.984	36.941	2.31	2.30	10.0	91.52	9.94	91.52	0.0
37.0	36.961	36.938	2.31	2.30	10.0	84.39	9.87	84.40	25.0
37.0	36.601	36.579	3.46	3.47	10.0	62.87	10.03	62.98	50.0
37.0	36.832	36.835	1.50	1.51	20.0	91.29	19.99	91.38	0.0
37.0	37.006	37.011	1.64	1.63	20.0	84.12	19.96	84.12	25.0
37.0	36.715	36.718	2.20	2.20	20.0	62.54	20.04	62.64	50.0
37.0	37.114	37.120	1.13	1.13	30.0	89.99	30.00	89.92	0.0
37.0	37.117	37.128	1.48	1.48	30.0	82.85	29.88	82.79	25.0
37.0	37.077	37.088	1.66	1.65	30.0	61.45	29.98	61.40	50.0

Table 5-1 Simulation results for h-pol, no bias in T or T_b.

S - "true" sea surface salinity

T - "true" sea surface temperature

θ_i - incidence angle

T_b - L-band brightness temperature calculated from S, T and θ_i

T_{100} - mean of 100 simulated values of T with random errors and bias

T_{b100} - mean of 100 simulated values of T_b with random errors and bias

S_{avg} - value of S estimated using T_{100} and T_{b100}

S_{100} - mean value of S estimated from 100 individual retrievals using simulated T and T_b (with random errors and bias)

sd S - standard deviation of 100 estimated S values

rms S - rms difference between 100 estimated S values and true S

All simulations are for the L-band frequency 1.43GHz. See text for more details.

computed, such as skewness and kurtosis, and the form of the distributions of S were examined. The results show that:

a) The errors in the retrieval of S are smaller in the case of uniform errors in T and T_b, than if those errors are normally distributed. This is unsurprising, as the variance for the normal case is twice that for the uniform (the errors in the normal case are $\sim\sqrt{2}$ larger than in the uniform case; that is, they seem to scale with the standard deviations of T and T_b).

b) The resulting distributions of S are approximately uniform, if the errors in T and T_b are uniform, and approximately normal if the errors are normal. This can be deduced for the values of skewness and kurtosis of the distributions and by visual inspection of the plotted histograms of S (not shown). The implications of this will be considered further below.

On the basis of these initial simulations, all succeeding simulations were carried out using normally distributed errors in T and T_b with standard deviation of 0.8165K.

The results for the simulations with n = 100 are presented in Tables 5-1 to 5-10. Tables 5-1 and 5-2 present the results for h-pol and v-pol retrieval of S with random errors but no biases in T or T_b. Tables 5-3 to 5-6 are for h-pol with random errors and biases in T_b of 0.5K and -0.5K, and in T of 0.5K and -0.5K, respectively (simultaneous biases in T and T_b are not considered). Tables 5-7 to 5-10 give similar results for v-pol. Note that the error in the estimate S_{100} is the standard deviation (sd) of S divided by $\sqrt{n}$ (=10).

From these results the following can be deduced:

a) the h-pol errors increase with increasing θ_i and decreasing T, showing little change with changing S.

b) the v-pol errors increase with decreasing θ_i and decreasing T, showing little change with changing S.

c) for both h- and v-pol a ±0.5K bias in T_b degrades the recovery of S significantly, while a similar bias in T has a much smaller impact.

d) for both h- and v-pol retrieving S from averaged values of T and T_b (T_{100}, T_{b100} giving S_{avg} in the tables) results in estimates that differ little from retrieving S from individual T and T_b values and then averaging (S_{100} in the tables).

e) the standard error of the estimate S_{100} (sd S / $\sqrt{n}$) varies from 0.08 to 0.54psu, and if the low temperature case (T = 0°C) is excluded, then the values are more typically in the range 0.1 to 0.3psu.

5.1.2 Key to tables of simulation results

that the basic retrieval accuracy using a single measurement is of the order of 2 psu (Swift (1993)). As suggested by previous studies (Lagerloef *et al.* (1995), Srokosz (1995)) it will be necessary to average in both time and space to retrieve useful measurements of S in the open ocean. If the ocean were unchanging (that is, T and S at any location remain constant over the averaging period) and the errors in T_b and T were simply random (no biases), then the most accurate retrieval might be obtained by averaging T_b and T and inverting Eq. 5-1 to obtain S. This is clearly not the case in general. The simulations carried out and described here will examine the effects of both random errors and biases in T_b and T on the retrieval of S.

On the basis of earlier studies (Lagerloef *et al.* (1995), Srokosz (1995)) a typical number of observations that might be averaged would be of order 100. For example, assuming that the instrument has a footprint of 30km and a re-visit time of 3 days, we would have O(100) samples for a 200km x 200km x 10day average (GODAE) or for a 100km x 100km x 30day average (Levitus). So for the simulations here that will be the number n used in the majority of cases. No attempt has been made to account for the possibility of multiple measurements that an instrument like MIRAS could make of the same area of the ocean at different incidence angles, due to its 2-D imaging capability.

Simulations are based on Eq. 5-1 with an initial value of T and S, from which T_b is calculated. For each simulation random errors and / or biases are added to the T and T_b values n times and S is retrieved for each case. A simple nonlinear solver is used to obtain S from Eq. 5-1 given the values of the other variables. The resulting n values of S are averaged and various statistics are calculated (mean, standard deviation, rms error). In addition, for comparison, the n values of T_b and T, with added errors and/or biases, are averaged and S retrieved.

The simulations were carried out for values of S = 33, 35, 37 psu, which are typical of the open ocean (see Srokosz (1995) and Levitus *et al.* (1994)), and T = 0, 10, 20, 30°C (also the range found in the open ocean). Three incidence angles (θ_i = 0°, 25°, 50°) are used in the simulations, covering the range typical of instruments like MIRAS (Goutoule (1995)) or ESTAR (Swift (1993)). As noted earlier, the frequency is chosen to be 1.43GHz (L-band) and both horizontal and vertical polarisations are considered. Before discussing the results presented in Tables 5-1 to 5-10, where each simulation uses n = 100 retrievals (for each value of S, T, θ_i, and *pol*), some conclusions from simulations using n = 1000 retrievals, which are probably more statistically stable but less relevant to actual retrievals, will be discussed.

For n = 1000, simulations were carried out where both uniform and normal error distributions were assumed for T and T_b. In the uniform case errors were assumed to be uniform in the range ±1 K, in the normal case errors were assumed to have a variance twice that of the uniform case (2/3; implying a standard deviation of 0.8165K).[1] From these initial simulations various statistics of the retrieved S were

[1] To some degree this choice is arbitrary. Using the same variance as the uniform case would give a standard deviation of 0.5774 K. This seemed too small, in view of the oft-quoted error of ±1K in T_b. Using a standard deviation of 1 K would correspond to 3 times the variance of the uniform case. The errors in the estimated S would appear to scale with the standard deviation of the errors in T and T_b, which in itself says something about the retrieval.

breaking waves (Hollinger (1971), Webster & Wilheit (1976), Lerner & Hollinger (1977), Blume *et al.* (1978), Skou (1995)). Therefore the largest uncertainty in any attempt to measure SSS using L-band may arise from these wind speed dependent effects. The impact of T on S estimation has been calculated by Swift & McIntosh (1983) for L-band to be 0.4 to -0.2 psu per °C over the T range 0 to 30°C. Therefore accurate measurements of T are required to retrieve S.

At a minimum it will be necessary to have independent T and wind speed measurements, in addition to T_b at L-band, in order to retrieve S. With a single frequency radiometer it will not be possible to measure all the parameters required for the retrieval. Ideally, simultaneous (meaning on the same satellite and looking at the same piece of ocean as the L-band radiometer) measurements of T and wind speed would allow for the best retrieval of S (airborne systems have measured T using infrared radiometers; Miller *et al.* (1998)). Nevertheless, even in the absence of such simultaneous measurements, by using data from other satellites it should prove possible to obtain useful retrievals of SSS. SST data are, or will be, available from AVHRR, ATSR-2, AATSR and AMSR, and wind speed data from AMI, SeaWinds and ASCAT, SSM/I, AMSR (plus altimeter missions). Clearly these measurements will not in general be made simultaneously with any L-band radiometer ones, and it is necessary to investigate how best to combine these data to optimise the retrieval of SSS. It should be noted that Lerner & Hollinger (1977) were able to recover S estimates from the Skylab 1.4GHz radiometer using a combination of modelling and ancillary data on T and wind speed. Though somewhat crude, their approach shows that it is possible to retrieve S spaceborne passive microwave radiometer measurements.

5.1.1 Simulating the retrieval of S from L-band brightness temperatures

There are many effects that might influence the retrieval of S from L-band brightness temperatures (see Swift & McIntosh (1983)). Due to lack of knowledge about some of these effects (wind, foam, rain) it is not possible to include them easily in a simulation of the retrieval of S. Therefore, here a simple simulation will be carried out that examines the retrieval of S from the L-band brightness temperature, based on the equations of Klein & Swift (1977) and Swift & McIntosh (1983). These allow the brightness temperature T_b to be written as

$$T_b = e(T, S, f, \theta_i, pol)\, T \qquad \textit{Eq. 5-1}$$

where the emissivity e is a function of the sea surface temperature T, the sea surface salinity S, the frequency f (here L-band, 1.43GHz), the incidence angle θ_i and the polarisation (*pol* - horizontal or vertical). Details of the equations used can be found in the appendix, Section 5.2.7. Assuming that f, θ_i and *pol* are known properties of the instrument, the retrieval of S requires knowledge of T_b and T. As T_b is measured by the instrument, it is clear that an independent measurement of T is required to retrieve S. Here it will be assumed that an independent measurement of T is available, then the effect of errors in T_b and T on the retrieval of S will be examined.

The first point to note is that Eq. 5-1 is nonlinear in T and S. Therefore, errors in T_b and T may not translate in a simple way into errors in S. Hence the need to carry out simulation studies. Typical errors in T_b and T might be of order 1 K, and this means

5 Retrieval of sea surface salinity from L-band passive microwave radiometer measurements

5.1 Introduction

The sensitivity of L-band (1.43GHz) passive microwave measurements of oceanic brightness temperature to sea surface salinity S is well established (Lagerloef *et al.* (1995)) and its use for the measurement of S from aircraft has been demonstrated (most recently by Miller *et al.* (1998)). The brightness temperature $T_b = eT$, where T is the sea surface temperature (SST), and e is the emissivity. e is a function of the dielectric constant, incidence angle, polarisation, and other factors. The dielectric constant for sea water depends on both S and T (Klein & Swift (1977), Swift & McIntosh (1983)). Therefore, in principle, it should be possible to obtain S information from L-band passive microwave measurements if the other factors influencing T_b can be accounted for (this point will be considered further below). If this is the case then the sensitivity of the 1.43GHz T_b to S is 0.5K per psu for an T of 20˚C decreasing to 0.25K per psu for an SST of 0˚C, for an incidence angle of 0˚ (Skou (1995), Lagerloef *et al.* (1995)). This will make retrieval of SSS more problematical at higher latitudes where the ocean is colder.

Assuming that the instrument can measure T_b to 1 K, it is clear that from a single measurement SSS cannot be recovered to the accuracy obtained using conventional means of measuring salinity. However, if the errors contributing to the 1K uncertainty in T_b are random, then useful SSS data may be obtained by averaging the individual measurements in both space and time (Lagerloef *et al.* (1995), Srokosz (1995)). Note that the GODAE optimised requirement is 0.1psu over 200km boxes over 10 days, and the threshold requirement is 1psu, over 500km boxes, over 10 days (see Table 3- and http://www.bom.gov.au/bmrc/mrlr/nrs/oopc/godae/spacereq.html; also IOC/WMO, 1998). For this study, assuming an instrument with a footprint of 30km and a re-visit time of the 3 days, averaging over 200km boxes and 10 days should allow the GODAE optimised requirement of 0.1psu to be met, except possibly at high latitudes. Monthly averages over 100km boxes should give data comparable to the standard climatologies, such as Levitus *et al.* (1994). This retrieval problem will be investigated further through the use of simulations (see below).

As noted above, it is necessary to account for the other factors that influence T_b in order to measure S. These include, T, surface roughness, foam, sun glint, rain, ionospheric effects and galactic/cosmic background radiation. Estimates for the uncertainties associated with some of these have been made (see, for example, Swift & McIntosh (1983) and Lagerloef *et al.* (1995)). Sun glint is best eliminated by discarding affected data. The effect of rain on the brightness temperature at L-band has been estimated to be ~ (0.01 R H) K, where R is the rain rate in mm/hr and H is the height of the rain column in km (Lagerloef, pers. comm.). Typically, H is 1 to 5km and R is 1 to 100mm/hr (light rain to tropical downpour), so the brightness temperature might increase by 0.01 to 5K. Some correction for this effect might be possible using other satellite observations of rain (alternatively, data affected by heavy rain would need to be discarded). Surface roughness and foam are usually considered together as a wind speed dependent effect. They are not well characterised for L-band. Their impact on the brightness temperature has been variously estimated to be in the range 0-0.4K per m s^{-1}, depending on incidence angle, polarisation and the presence/absence of

Two different configurations are simulated, the first one including only 1.4 and 6.8 GHz channels, and a second one that includes a channel at 2.65 GHz. The calculations show that both, horizontally as well as vertically polarized brightness temperatures must be measured to obtain reasonable retrievals. To make useful measurements of *S* it is necessary to have at least dual polarized measurements at two frequencies near 1.4 and 6.8 GHz. The inclusion of a channel at 2.65Ghz is useful only if the noise can be reduced to values below 0.2 K. At smaller noise levels one could take advantage of accurate surface temperature and wind speed measurements. The latter are the more important ones. If one could obtain wind speed fields with an accuracy better than 0.5 m/s and temperature fields with an accuracy of 0.5 K then the salinity could be retrieved with an error well below 0.4 psu. It is important that the single measurements have a noise below 0.5 K and an average over more than 100 brightness temperature measurements can be built.

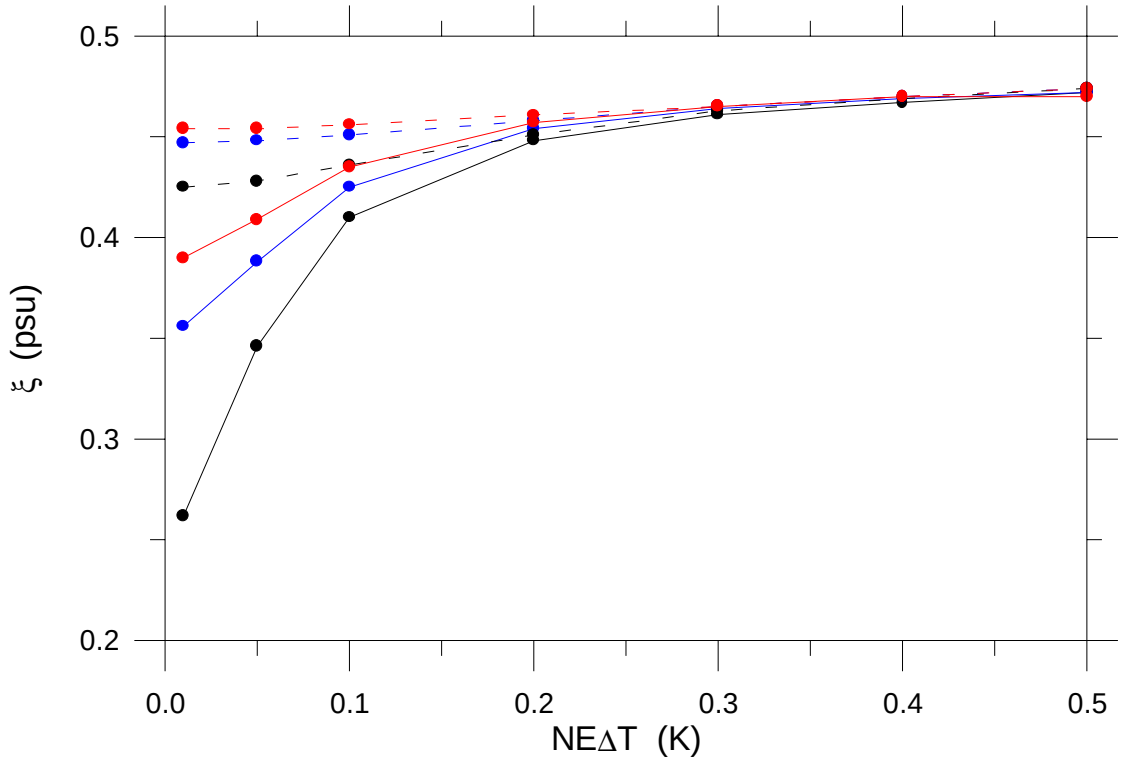

Figure 4-7 Retrieval error of surface salinity as function of radiometric noise, contiguous lines are for retrievals including 1.4, 2.65, and 6.8 GHz measurements, dashed lines are for retrievals excluding the 2.65 GHz channel; the assumed error in surface temperature and wind speed are 0.5 K and 1.0 m/s (red), 0.5 K and 0.5 m/s (blue), 0.3 K and 0.1 m/s (black).

The assumptions made about the accuracy of sea surface temperature and surface wind speed seems to be very demanding. However, it should be kept in mind that this accuracy is not needed for a single measurement but for a spatial and temporal average. For example, in the case of the GODAE requirements an average of 200 km and 10 days is considered. On this scale an accuracy of 0.5 K for the surface temperature and 0.5 m/s for the surface wind speed is not beyond the scope of today's capabilities of measuring these parameters from space.

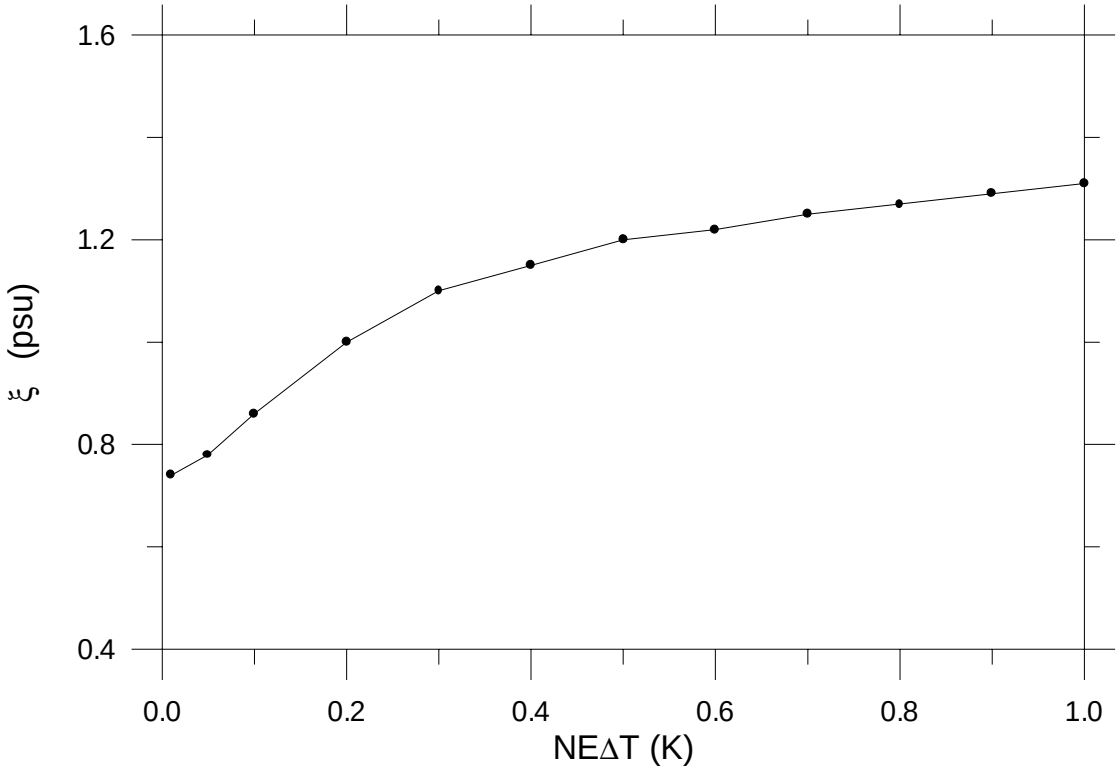

Figure 4-5 Retrieval error of surface salinity as function of noise equivalent temperature difference assuming a measurement of brightness temperatures at 1.4, 2.65, and 6.8 GHz and a knowledge of surface temperature (0.5 K error) and of surface wind speed (0.5 m/s error).

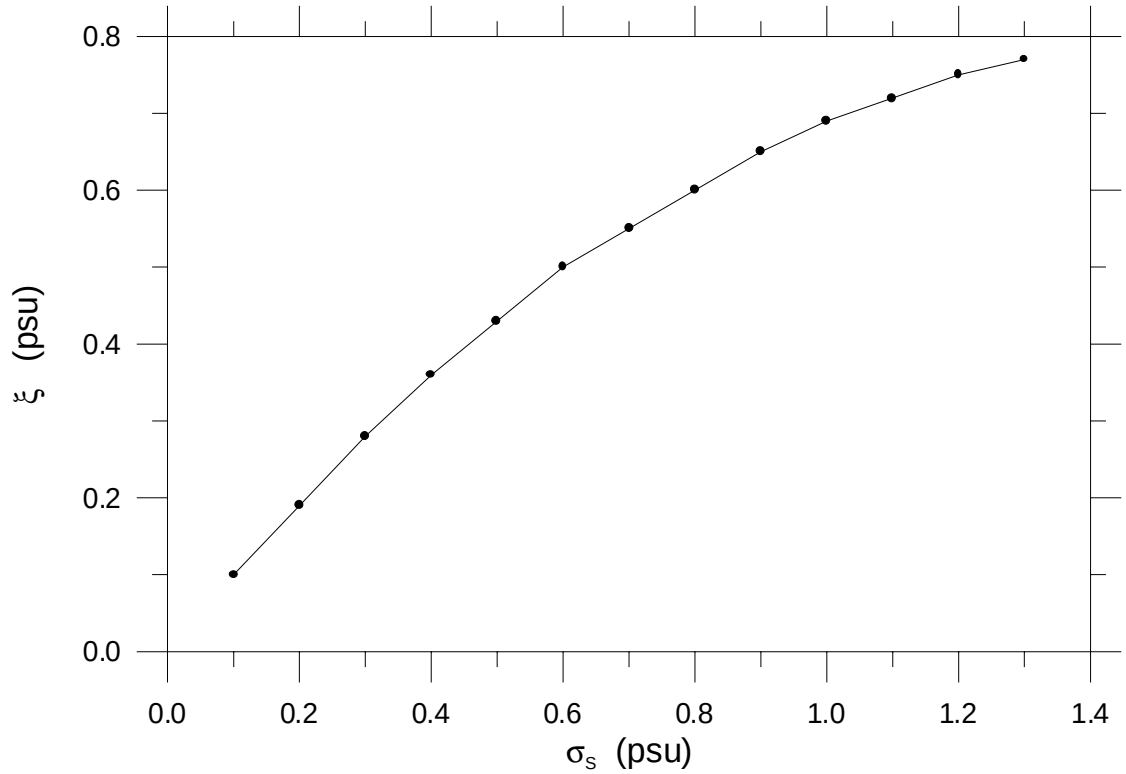

Figure 4-6 Retrieval error of surface salinity as function of an a-priori knowledge of S assuming an instrumental noise of 0.2 K for brightness temperatures at 1.4, 2.65, and 6.8 GHz.

The global simulations carried out for 1012 different situations for the frequencies 1.4, 2.65, and 6.8 GHz are analysed by linear multivariate regression and by means of an artificial neural network aiming at a retrieval of the surface salinity from the synthetic measurements. Radiometric noise has been included by normally distributed random values with zero mean and standard deviation corresponding to the assumed noise equivalent temperature difference (NEΔT). Initial results obtained show that the non-linear neural network is not superior to the linear method since only slight non-linearity is involved. Therefore, all results presented here are taken from the linear regressions.

In a first step it is assumed that absolutely no a-priori knowledge about the surface salinity is available, hence it could take any value between 32 and 37 psu (the total range assumed here). The corresponding retrieval error, ξ, assuming measurements at 1.4 GHz only and without radiometric noise are of the order 1.4 psu for the incidence angles θ = 0°, 25°, and 50°. Inclusion of additional knowledge about surface temperature *T* and wind speed *u* slightly improves the retrieval accuracy to ξ = 1.2, 1.2, and 1.0 psu for θ = 0°, 25°, and 50°, respectively, if the standard errors of *T* and *u* are kept below 0.5 K and 1.5 m/s, respectively. Further reduction of the retrieval error is only possible by including additional measurements at 2.65 and 6.8 GHz. Still, the knowledge about *T* and *u* has to be included at a level of 0.5 K and 0.5 m/s, respectively. Figure 4-5 shows the retrieval error as function of NEΔT (same for all channels). The incidence angle chosen here is θ = 50°. Without radiometric noise the salinity is obtained with an accuracy of 0.74 psu. An increase of the NEΔT to 1.0 K renders the additional information from the 2.65 and 6.8 GHz measurements useless.

Better results are obtained if an a-priori knowledge of *S* is assumed. As the salinity does not vary everywhere between 32 and 37 psu but changes within smaller bounds around a local mean it is realistic to include this information. Depending on the accuracy of the a-priori knowledge about *S* the combined retrieval using this a-priori knowledge together with dual-polarized satellite measurements at 1.4, 2.65, and 6.8 GHz gives values of ξ as shown in Fig. 4-6. A NEΔT = 0.2 K is assumed for all channels. No information about surface temperature or wind speed is used here. It is seen that the satellite measurements explain a substantial part of the salinity as long as the a-priori knowledge remains above 0.4 psu. If having a better a-priori information than this the improvement by the measurements becomes marginal.

In the following it is assumed that *S* is known a priori with a standard error of 0.5 psu. Based on this it is calculated to what extent the surface salinity can be retrieved at different radiometric noise and with different information about the sea surface temperature and the surface wind speed (Fig. 4-7). While it is clear that the radiometric noise cannot be as small as the values adopted here it is assumed that the noise can be reduced by horizontal averaging of single brightness-temperature measurements.

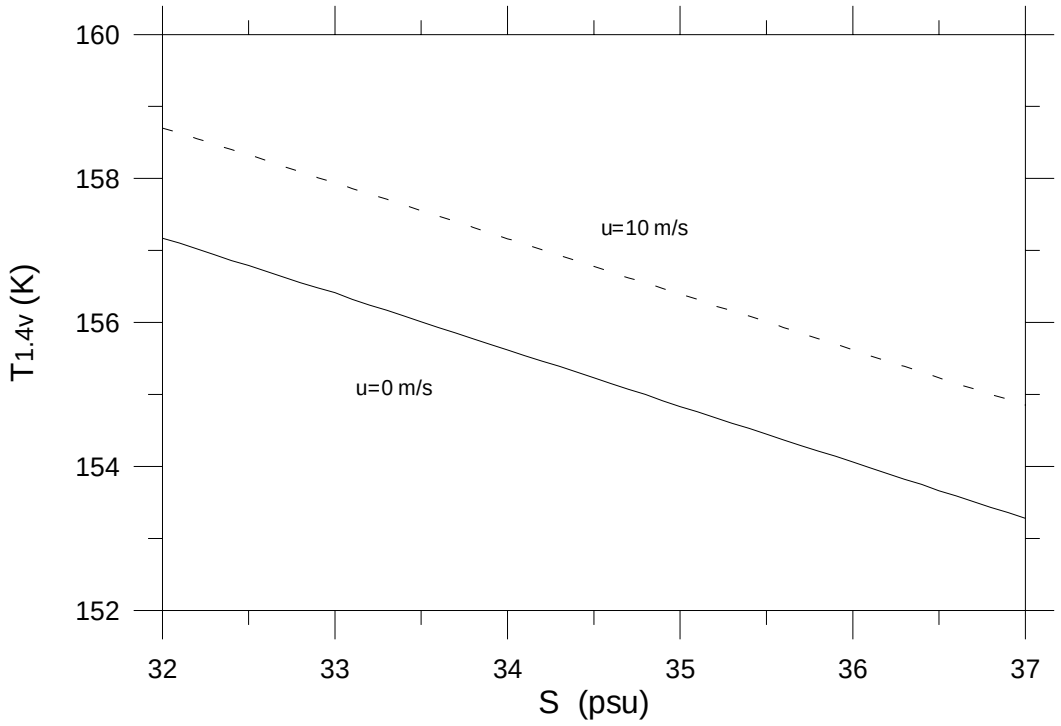

Figure 4-3 Variation of vertically polarized brightness temperature at the top of the atmosphere as function of sea surface salinity for two wind speeds, the atmospheric situation represents a tropical atmosphere with 38 kg/m^2 water vapour, 122 g/m^2 liquid water and a surface temperature of 293.71 K.

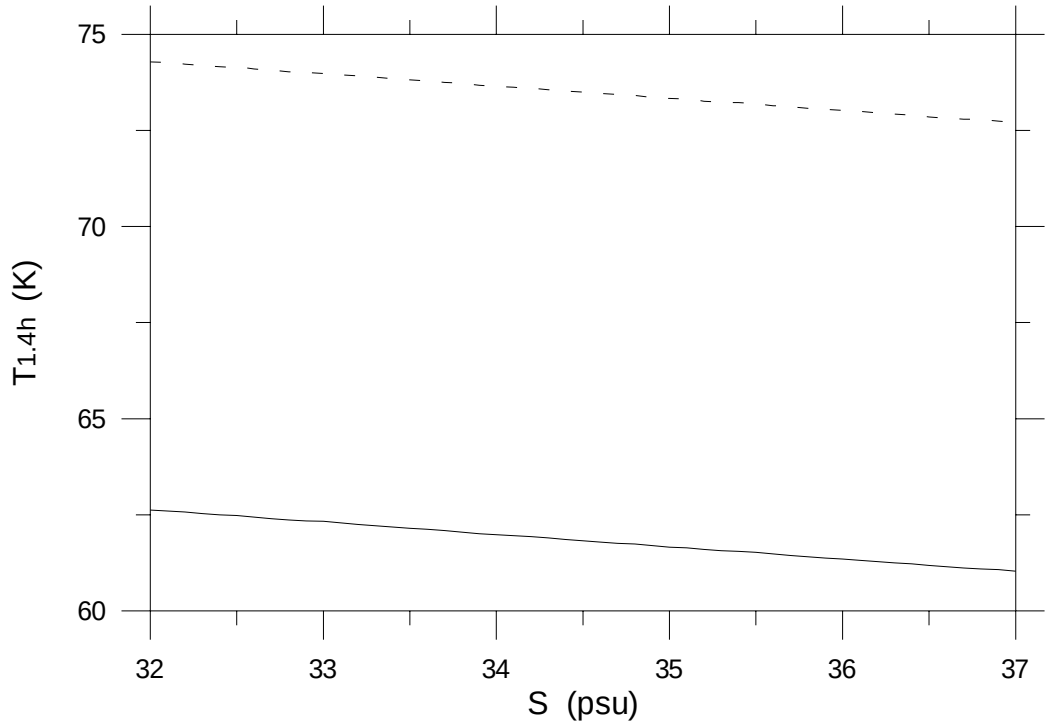

Figure 4-4 As figure 3, but for horizontally polarized brightness temperature.

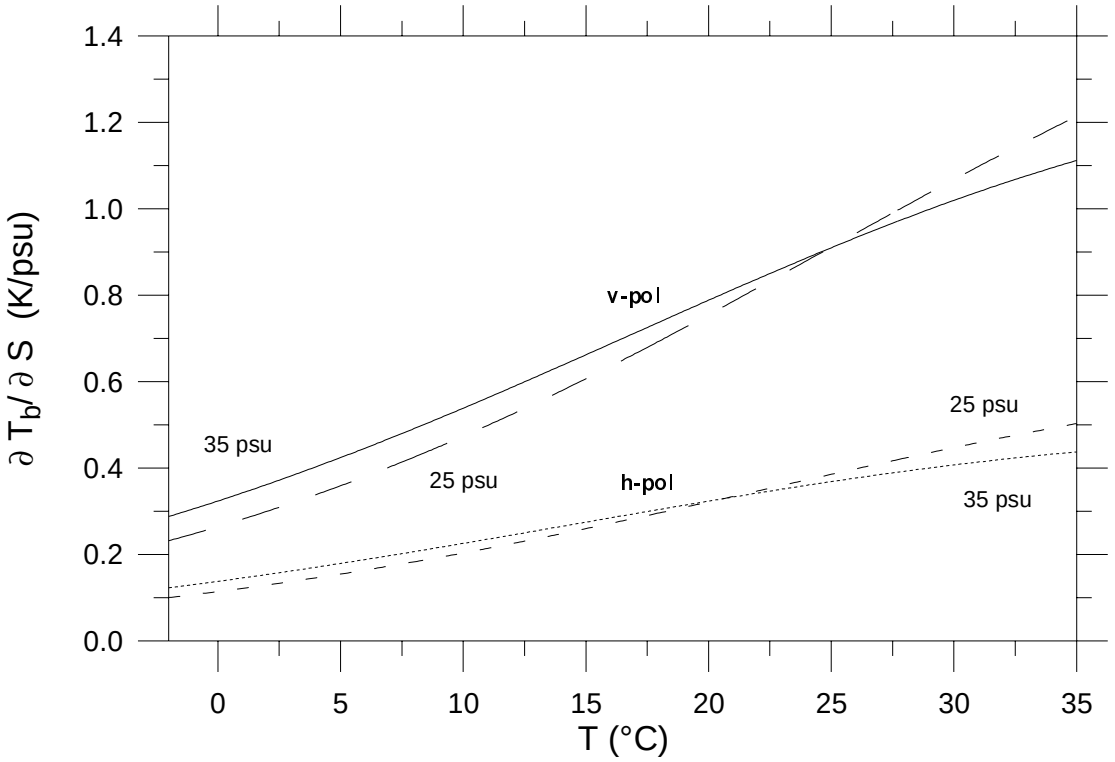

Figure 4-1 Variability of surface emission at 1.4 GHz with respect to surface salinity as function of surface temperature at vertical and horizontal polarization and at two surface salinities of 25 and 35 psu, the wind speed is 0 m/s.

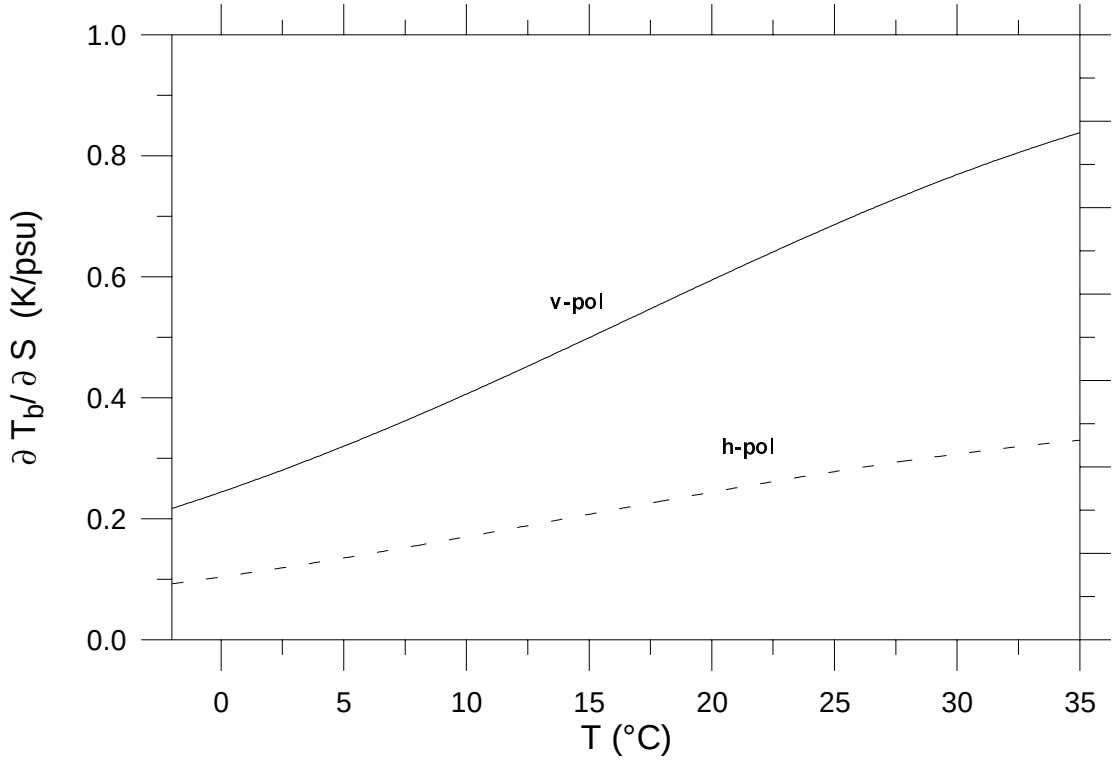

Figure 4-2 Variability of brightness temperature with surface salinity as function of surface temperature at a salinity of 35 psu and a wind speed of 25 m/s.

The assumption $\rho = (1-\varepsilon)$ is only true in the case of specular reflection. For the rough surface radiation from all directions can be reflected into the direction specified by the observation angle θ. Therefore, a correction is necessary to account for the contribution of diffusely reflected radiation, depending on surface roughness and optical depth of the atmosphere. For this we make use of the parameterisation given by Guissard et al. (1994). For the calculation of the atmospheric attenuation the millimeter propagation model described by Liebe (1989) is used.

The simulation of the global variability of the satellite-measured radiation field is performed for a set of 1012 globally distributed marine radiosonde profiles, including vertical temperature and humidity distributions as well as surface temperatures. Cloud liquid water has been inserted into the profiles where the relative humidity exceeds 96%. A normally distributed random liquid-water density is chosen with a mean of 0.1 g/m³ and a standard deviation of 0.1 g/m³. Values below zero are set to zero. The wind speed is taken randomly from a Rayleigh distribution with a mean of 7.5 m/s. The salinity included in the simulations is selected randomly from an uniform distribution between 32 and 37 psu.

Before commencing with the global simulations a few sensitivity studies have been carried out in order to demonstrate how the surface salinity modifies the upwelling radiation field at the sea surface. Figure 4-1 shows the variability of the brightness temperature at an incidence angle of 50° with respect to the surface salinity $\partial T_b/\partial S$ at a wind speed of 0 m/s. It is seen that the brightness temperature almost linearly increases with the salinity at both vertical and horizontal polarization. The variability is slightly dependent on the salinity itself, showing higher sensitivity at higher salinity for temperatures below about 20 to 25 °C and the contrary behaviour at higher temperatures. At increasing wind speed the sensitivity of the brightness with respect to the surface salinity is reduced, mainly at high temperatures and vertical polarization as shown in Fig. 4-2 for a salinity of 35 psu.

At the top of the atmosphere the brightness temperatures at 1.4 GHz decrease with increasing salinity as shown for a tropical situation in Figs. 4-3 and 4-4 at vertical and horizontal polarization, respectively. The brightness temperatures increase while the surface emissivity increases with the wind. The atmospheric effect included here is an attenuation of the surface emission by 1.3 K at vertical and 1.0 K at horizontal polarization. On the other hand the brightness temperature measured at the top of the atmosphere is enhanced by an atmospheric emission of 3.9 K and its reflected downwelling part amounts to 1.9 K at vertical and 3.4 K at horizontal polarization.

absorption, and reflection. The brightness temperature $T_{\nu\zeta}$ at frequency ν and polarization ζ can be expressed as (e.g. Schlüssel and Emery, 1990)

$$T_{\nu\varsigma} = \varepsilon_{\nu\varsigma} T_0 \exp(-\delta_\nu^* / \cos\theta) + \int_0^{\delta_\nu^*} T(\delta_\nu) \exp(-\delta_\nu / \cos\theta) d\delta_\nu +$$
$$(1-\varepsilon_{\nu\varsigma}) \exp(-\delta_\nu^* / \cos\theta) \int_{\delta_\nu^*}^{0} T(\delta_\nu) \exp(-\delta_\nu / \cos\theta) d\delta_\nu + T_{Sp} \exp(-2\delta_\nu^* / \cos\theta)(1-\varepsilon_{\nu\varsigma}) \quad \textit{Eq. 4-1}$$

where the terms on the right side describe

1. the radiation emitted by the surface at temperature T_0 at an emissivity $\varepsilon_{\nu\zeta}$ transmitted through the atmosphere with optical depth δ^*_ν at an incidence angle of θ to the satellite,
2. the radiation emitted by the atmosphere at temperature T to the satellite,
3. the downward atmospheric emission reflected by the surface and transmitted to the top of the atmosphere, and
4. the galactic space emission transmitted through the atmosphere, reflected by the surface and transmitted to the satellite.

At 1.4 and 2.65 GHz, the contributions from terms 2 and 3 are small and often neglected. However, for an accurate calculation of the brightness temperature at satellite altitude they have to be included. The contribution is mainly due to the air absorption continuum which depends on atmospheric pressure, temperature and humidity. While term 2 accounts for a contribution of 3.5 to 5 K at 1.4 GHz, the magnitude of term 3 depends on the polarization. At horizontal polarization its contribution amounts 3 to 4 K, at vertical polarization only about 1.5 to 2 K. The transmission of the surface-leaving radiation through the atmosphere is of the order 98.5% at a frequency of 1.4 GHz and an incidence angle of 50°. Although the total amount of the atmospheric emission and its reflected part are an order of magnitude smaller than the surface emission their variability is greater than the signal due to salinity changes that is to be retrieved.

The surface emissivity is described according to Pandey and Kakar (1982):

$$\varepsilon_{\nu\varsigma} = (\varepsilon_{\nu\varsigma S} + \Delta\varepsilon_{\nu\varsigma}(u))(1 - f(u)) + \varepsilon_{\nu\varsigma f} f(u) \quad \textit{Eq. 4-2}$$

where $\varepsilon_{\nu\varsigma S}$ is the specular emissivity of the smooth surface, $\Delta\varepsilon_{\nu\varsigma}(u)$ is the change in surface emissivity due to the wind-roughned, not with foam covered surface at wind speed u, $\varepsilon_{\nu\varsigma f}$ is the emissivity of foam and f is the fractional foam coverage. It is assumed that the surface reflectivity is $\rho=(1-\varepsilon)$. The specular reflectivity is calculated using the Fresnel formulae with a temperature, salinity and frequency dependent dielectric constant of sea water as specified by Klein and Swift (1977). The variability of the surface emissivity by wind-roughening and foam at frequencies below 6.8 GHz (not considered by Pandey and Kakar) is included according to Webster and Wilheit (1976).

- Initial conditions for climate forecasts aiming at a prediction of western boundary currents, seasonal prediction, and climate change forecast.

- Sustain and design for a permanent global ocean observing system including remote and direct measurements for GOOS, GCOS, operational oceanography, and multi-purpose applications.

For the remote sensing of *S* a requirement is given for studying circulation and water transport. The required accuracy is 0.1 psu at a horizontal resolution of 200 km and a temporal resolution of 10 days. This would be optimum. A relaxed threshold requirement is 1 psu at 500 km and 10 days, see Table 3-2.

Table 3-2 GODAE requirements for sea surface salinity.

	Optimised requirements	Threshold requirements
Spatial resolution (km)	200	500
Temporal resolution (days)	10	10
Accuracy (psu)	0.1	1.0

3.9 Requirements of commercial users

A variety of commercial users would benefit indirectly from space-borne ocean salinity measurements. Results from regional ocean circulation models will be improved and be of enhanced value for fisheries, coastal shell-fisheries, harbor and bridge construction companies, oil exploration companies and water pollution management. By the same token the results from global, coupled ocean-atmosphere climate models will produce enhanced inter-annual climate predictions, such as El-Niño forecasts. These will be of great value for many areas, covering fisheries, agriculture, fire prevention etc. on a quasi global scale. As these users do not benefit directly from the salinity measurements but from secondary products (e.g. forecasts made by national agencies or even international entities), detailed requirements for the "commercial users communities" cannot be given. With respect to the secondary nature of the commercially utilised products the resulting requirements should be the same as those specified in Table 3-1.

4 Variation of the Radiation Field due to Salinity Changes and Multispectral Retrieval of the Surface Salinity

The impact of sea surface salinity changes on the radiation field at the sea surface and at satellite altitude is studied by means of radiative transfer simulations. The radiative transfer equation is integrated ignoring atmospheric scattering processes, thus, allowing only atmospheric absorption and emission as well as surface emission,

S have also been observed in the Gulf of Panama, where low salinity (<30 psu) was replaced by water with enriched salinity of more than 34 psu during the course of an ENSO cycle (Donguy, 1994). Details of these changes need to be investigated.

3.7 Impact of surface salinity on numerical weather forecast

The numerical weather forecast predicts the atmospheric circulation on time scales below about two weeks. Within these time scales salinity changes happen, but their effect on the air-sea exchange and therefore on the atmospheric circulation is rather small.

3.8 Assimilation of Salinity in Ocean Models

The assimilation of surface salinity fields in numerical models of the ocean would be of benefit for improving models and/or parameterisations of the upper mixed layer of the ocean and for the calculation of surface fluxes (Acero-Schertzer et al., 1997). They compare the oceanic surface currents as found in the National Centers for Environmental Predictions's (NCEP) ocean analysis against surface mixed layer current observations and show that the four-dimensional NCEP analysis does not correctly account for observed temperature-salinity correlations because of a lack of surface salinity observations. As a consequence the analysis displays erroneous pressure gradients that drive unrealistically strong geostrophic currents and force large accelerations in the western boundary of the Pacific Ocean. The authors state that salinity observations seem essential for accurate analyses of anomalies.

The availability of *S* with accuracy between 0.05 and 0.1 psu at a horizontal resolution of 1° would provide a substantial information to improve the modelled wind-driven circulation in the subtropical ocean. At higher latitudes an accuracy of 0.01 to 0.02 psu might be necessary to get an insight into the deep and intermediate water formation. However, great salinity anomalies as described above show a variability of the order 0.5 to 1 psu.

The Global Ocean Data Assimilation Experiment (GODAE) is an experiment that has been set up in 1997 by the Ocean Observations Panel for Climate (OOPC) supporting the WCRP, GOOS, and GCOS. GODAE's task is to demonstrate the feasibility and practicability of routine, real-time global ocean data modelling and assimilation systems. The concept of GODAE is built by opportunity and need (Smith, 1997). The needs, clearly stated, partly consist of investment in global observing to support the following objectives:

- Extended predictability of coastal and regional sub-systems for coastal forecast systems, regional monitoring, and prediction.
- Provide several to 20 days high-resolution, upper-ocean forecasts and nowcasts for ship routing, transport, safety at sea, and naval applications.
- Integrated analyses for research and development as well as reanalysis for the international research programmes CLIVAR, GLOBEC, ... to test hypotheses and to conduct process studies.

strong salinity front between the western Pacific freshwater and the central Pacific water. The front is thought to be related to the large-scale convergence between salty westward directed south equatorial current and the eastward propagation of low salinity water associated with the reverses of the easterly winds in the warm pool (Picaut et al., 1996). The front was found to be highly mobile in the model simulations. However, this could not be confirmed by any observations. While the front itself had been observed its mobility could not be identified because of poor temporal and spatial resolution of the measurements. Maximum salinity gradients found in the simulated front are of the order 0.2 psu per degree longitude. Observations suggest only 0.13 to 0.17 psu (Eldin et al., 1998, Kuroda and McPhaden, 1993, respectively). Monthly variations found around the salinity front in the model results range from about 0.1 to 1 psu in the mixed layer salinity.

During the 1982/83 El Niño, a low S anomaly was observed propagating eastward along the equator. The phase speed of this anomaly was ~0.3 cm/s which resulted in salinity changes of > 0.5 psu per month (Dessier and Donguy, 1987).

Most salinity measurements stem from dedicated field experiments. Few programmes like SURTROPAC (Donguy, 1994) have been launched to utilise voluntary observing ships for surface salinity measurements. While the field experiments are restricted to both, short time periods and small areas, the routes of the voluntary observing fleet are fixed to certain tracks between ports; wide areas are not covered at all. Typical errors of operational salinity measurements taken from ships of opportunity with the bucket method are of the order 0.1 psu (Delcroix and Hénin, 1991). For a monthly mean of a 2° latitude by 10° - 15° longitude grid box the root mean square error is reduced by a factor of ~2.5, assuming 6.1 samples per month in this grid box. This value sets a reference against which possible satellite measurements of S have to be compared.

However, a seasonal cycle of S could be described by the available measurements and also main climatological characteristics have been summarised, like the minima of S related to the ITCZ and SPCZ where rainfall dominates the surface freshwater flux. Further features can be linked to the atmospheric circulation patterns, like the weak wind associated with the anticyclone over East Asia leading to a maximum of S near 25° W off the Asiatic continent. Oceanic currents cause advection of salinity (e.g. low salinity advected by the Kuroshio to the vicinity of Japan as described by Donguy, 1994). Hence, the general salinity patterns mirror the prevailing features of the general circulation of the ocean and also partly of the atmosphere. But, there is a great space and time variability of which little is known so far because of sparse observations. For example, during El Niño years the climatic conditions change dramatically in the Pacific Ocean, leading to a replacement of the equatorial salinity minimum by a maximum. At the same time also the western Pacific salinity minimum south of 10° S is replaced by a maximum (Delcroix and Hénin, 1991). This evolution of different salinity states is linked to changes in the E-P balance during an ENSO cycle. Therefore, the surface salinity properties play an important role in the climate variation related to ENSO. A subtropical area with highest surface salinity is situated south of the Marquesas Isles near 15° S, 135° W. On the average, the salinity shows values greater 36.5 psu in this area, while it may drop below 36 psu in an El Niño phase. Donguy (1982) suggests that high salinity (>35 psu) in the tropical Pacific is an indicator for upwelling water at the equator and for droughts in the tropical region, while low salinity can be considered as an index of precipitation. Dramatic changes in

surface salinity that resemble the observed climate to initialise the oceanic model component but also to reduce the so-called coupling shock.

Experience with the open-ocean salinity restoring when tied to available, incomplete climatologies, however, demonstrates the need for more complete surface salinity fields. The weakness of the current coupled bulk flux forcing and effective restoring of surface temperature and salinity has been highlighted in the boundary current regions where poleward advection of positive temperature and salinity anomalies generates (through the open-ocean salinity restoring term) a net deposition of freshwater. This finding is opposite in sign to the response expected based strictly on physical principles (Doney et al., 1998).

Miller (1976) and Price (1979) showed in a one-dimensional model how rainfall over tropical and subtropical oceans can play a key role in varying the surface salinity and thus determining the temperature and depth of the entire mixed layer

3.6 Variability of surface salinity in the tropical ocean related to ENSO

The El Niño Southern Oscillation (ENSO) is an interannual phenomenon of the tropical Pacific Ocean with global importance (e.g. Wallace et al., 1998). Although the air-sea exchange of heat and the variability of sea surface temperature are mainly responsible for the ocean-atmosphere interaction in the tropical Pacific, the role of salinity and its change by freshwater fluxes at the sea surface have to be included for a full understanding of the entire ENSO process (Lukas and Lindstrom, 1991; Donguy, 1994). Much of the tropical Pacific Ocean is characterised by low wind speed and heavy rainfall. As discussed above, the net freshwater flux at the sea surface stabilises the upper ocean and makes it more sensitive to the low heat and momentum fluxes. Lukas (1990) suggests important feedback mechanisms between sea surface temperature, rainfall, near-surface salinity, and wind-induced mixing. Sea surface salinity measurements collected by voluntary observing ships have provided valuable insight into the near surface water mass variability and its relation to the atmospheric forcing in the tropical oceans. The strong seasonal to inter-annual variation of S is important to know and understand for a complete picture of ENSO (McPhaden et al., 1998).

Vialard and Delecluse (1998a) use an ocean general circulation model (OGCM) to study the effects of haline stratifications in the upper tropical Pacific Ocean on the low-frequency equilibrium of the COARE region. The model operates with a horizontal resolution of 1° in latitude and longitude. The sea surface salinity is a predictive variable in their model being extremely sensitive to the freshwater flux at the surface. A major uncertainty in the model study is the simulated circulation and thermohaline structure. Although they found a good large-scale structure correspondence of simulated and observed surface salinity a proper evaluation of the model results is hard because of sparse time-space coverage of salinity observations.

The variability of S in the tropical Pacific Ocean is discussed by Vialard and Delecluse (1998b). Their model study shows that the surface salinity varies most strongly in a narrow equatorial band between 2° S and 2° N. Annual as well as interannual events (like El Niño) alter the salinity more than 1 psu indicating the migration of the ITCZ in the annual cycle and the migration of the west Pacific warm/fresh pool in an El Niño/La Niña cycle. For the latter the one degree model resolution used reveals a

Timmermann et al. (1998) have shown from model results that positive surface temperature anomalies are associated with anomalously strong thermohaline circulation in the North Atlantic. The atmosphere's response to this is an enhanced North Atlantic Oscillation that in turn leads to anomalous freshwater fluxes off Newfoundland and in the Greenland Sea. The resulting surface salinity anomalies are advected by the sub-polar gyre and finally reach the convectively active region south of Greenland. Convection and following weakening of the thermohaline circulation reduces the poleward oceanic transport and subsequently forms negative surface temeprature anomalies. The duration of this cycle is roughly 35 years. Whether this process is associated with the great salinity anomalies observed is not yet clear.

3.5 Upper Ocean Salinity Boundary Condition Used in Models

A better understanding is necessary about the sea surface temperature – evaporation feedback that implies a temperature – salinity feedback. Usually, the difference between evaporation and precipitation, $E–P$, is fixed in large-scale ocean models (Hughes ad Weaver, 1996). This model set-up does not allow the description of the mentioned feedback and thus suffers from a lack of important model physics driving the ocean thermohaline circulation. Otherwise, the freshwater fluxes are often poorly known. They could be constrained by knowledge of S.

Chen and Rothstein (1991) postulated a barrier layer in the upper ocean: A shallow isohaline surface layer could be formed in response to forcing by $E–P$ resulting in a deep thermocline that is insulated from the surface layer by a barrier layer with no active turbulent mixing. The freshwater forcing has a potentially important role in ocean modelling and for a realistic inclusion of salinity in mixed layer models (Godfrey et al. 1998). This was demonstrated in several studies. Shinoda and Lukas (1995) used a Lagrangian model of the mixed layer in comparative studies with results from an Eulerian model to show how the horizontal advection of saline water from the central Pacific contributes to the maintenance of the thermohaline structure in the western Pacific warm pool. Sensitivity model studies of Webster (1994) highlight the influence of surface cooling by heavy rainfall on the mixed layer. Anderson et al. (1996) show that the thermodynamically active hydrological cycle of the western equatorial warm pool is important for the climate system. The inclusion of freshwater fluxes at the sea surface result in a much stronger local coupling between atmosphere and ocean than found in coupled models so far. The knowledge of the surface salinity could help to better specify the forcing in cases where $E–P$ is not known.

The initialisation of coupled climate models is a delicate problem which has not yet been solved completely. Modelers seek to minimise the drift in coupled general circulation models (CGCM) by obtaining initial conditions that satisfy the conditions of having the CGCM's fluxes dynamically and thermodynamically balanced. Climatically relevant adjustment time scales range from the order of days or months to decades (Mitchell and Dixon, 1997). When the ocean model components are exclusively forced by prescribed heat and freshwater fluxes there is no guarantee that the modelled surface conditions will resemble observed distributions as the ocean surface is not damped towards observations. Therefore, both, the restoration to observations of surface temperature and salinity as well as forcing with realistic surface fluxes are important. A well adjusted mix of both will offer the most realistic surface buoyancy forcing. Most of the CGCMs used today need initial fields of

3.3 River Discharge on the Continental Shelf

The variation of salinity due to freshwater discharge of rivers is important in continental shelf areas. At the surface the salinity gradient easily exceeds 6 psu per 100 km in the case of major rivers (Kourafalou et al., 1996). The actual salinity distribution, however, changes with time and depends on stratification of near-shore waters, prevailing wind speed and direction, and tidally induced water mixing. While the temporal variation of density distributions in the discharge areas can be used as tracer for the runoff it represents an important information about materials (trace elements, nutrients, sediments, radio-nuclides, and pollutants in general) that enter the coastal waters through river discharge. For most rivers the low-salinity area is confined to a region extending to about 150 km from the shoreline. Nevertheless, in situations with high river runoff and well developed low-salinity bands along the inner shelf, the model simulation occasionally show the formation of freshwater lenses that detach to the deeper shelf regions. Airborne microwave observations of S in the Chesaspeake outflow plume confirm these strong variabilities in coastal areas. A change of more than 10 psu over a distance of only 20 km have been observed in the first radiometrically produced image of surface salinity (Miller et al., 1998). Detached freshwater lenses drifting to the deeper shelf area show salinity differences of 1–2 psu from the surrounding ocean water.

The rivers, which are responsible for the main continental runoff, produce freshwater tongues and lenses spreading in coastal waters (Droppelman et al., 1970). While the freshwater lenses or tongues are rather stable features they are used as tracers for the oceanic circulation.

3.4 Great salinity anomalies

Widespread freshening of the upper 500-800 m layer of the northern North Atlantic happened in the period 1968 to 1982. According to Dickson et al. (1988) this event represents one of the most persistent and extreme variations in the global ocean climate observed so far. Beginning north of Iceland in the late 1960s this anomaly cycled around the Atlantic subpolar gyre for 14 years, finally returning to the Greenland Sea in the early 1980s. Greatest surface salinity anomalies of –1 psu were observed in the Labrador Current. Weaker anomalies, but still exceeding –0.1 psu, were found in the middle and eastern North Atlantic. Following this anomaly of the 1970s a further great anomaly has been identified in the 1980s (Belkin et al., 1998). An earlier great anomaly was observed between 1908 and 1910. However, no information is available about the real temporal and spatial extent of this earlier anomaly as no regular observations were made at that time.

Unanswered questions about the great salinity anomalies are related to their origin. It has not conclusively been proven whether the spreading of such an anomaly in the North Atlantic is due to advection of increased freshwater export from the Iceland-Greenland Sea (Dickson et al., 1988), excessive freshwater flux from the atmosphere to the ocean (Pollard and Pu, 1985) or an eastward shift of the North Atlantic Current (Martin et al., 1984). However, it is likely that the 1970s and the 1980s anomalies are of different origin (Belkin, 1998). The reason for the rather poor knowledge is a lack of complete and continuous survey of the ocean as salinity observations mainly depend on research cruises.

areas far from the rainfall event that produced the lens. The creation of the freshwater lenses depend on the distribution, strength, and duration of rainfall which all are rather poorly known (Lukas, 1990).

Soloviev and Lukas (1997) report about near-surface temperature-salinity fronts which are believed to be driven by gravitational spreading when other forces are absent. These fronts observed during COARE were modified subsequently by wind stress acting on the surface.

Besides the production of freshwater lenses that are characterised by lower salinity in the upper part of the oceanic mixed layer rainfall also creates a haline molecular boundary layer, a so-called freshwater skin (Schlüssel et al., 1997). The freshwater skin is only present during rainfall and exhibits salinity differences across the upper 30-50 μm of more than 2 psu during heavy rainfall and low wind-induced mixing.

Long-term average variations in *E–P* produce regional and basin-scale anomalies in sea surface salinity. This is clearly identified in mean salinity maps of the upper ocean (e.g. Levitus et al., 1994) where low salinity coincides with the precipitation maximum of the inter-tropical convergence zone (ITCZ) and South Pacific Convergence Zone (SPCZ). Enhanced salinity is present where excess evaporation occurs, mainly in the subtropical oceans and in areas with cold air outbreaks over relatively warm waters in parts of the polar oceans. Excess evaporation at the sea surface leads to areas with increased salinity which in turn drive intermediate and deep water formation. This is found to be most pronounced in the North Atlantic Ocean (GIN-Sea) and in the Weddell Sea where strong evaporation is accompanied by cooling of the sea surface which likely leads to the formation of sea ice. Both, evaporation and sea ice formation with successive brine release to the upper ocean cause an enhancement of the salinity in near-surface waters leading to a destabilisation of the upper ocean and possibly to deep convection (e.g. Rudels, 1990; Schauer 1995; Backhaus et al., 1997). However, the role of sea ice and brine release is not quite clear as pointed out by Schott et al. (1993). They deduced from observations that the intermediate convection in the central Greenland Sea during the winter 1988/89 was mainly thermally driven and no sea ice was involved. The variability of the surface salinity over a period of 4 months was about 0.3 to 0.5 psu at horizontal scales less than 100 km.

The convective mixing in the Greenland Sea causes a direct coupling of the surface layer to the subsurface layers during winter. In this way, surface temperature and salinity fronts may reflect the presence of subsurface fronts (van Aken et al., 1995) like the Arctic Frontal Zone, a quasi permanent feature in the Greenland-Norwegian Sea that extends roughly meridionally along 5° E from 72° N to 77° N. The surface salinity difference across the frontal zone is about 0.6 psu over a zonal distance of about 2° (corresponding to about 60 km at these latitudes). Meanders and eddies are associated with the front showing typical scales of 100 km and 40 km, respectively, with salinity changes of typically 0.2 psu.

Maximum seasonal salinity variations are found mainly in the ITCZ and the SPCZ. They are closely related to the seasonal rainfall patterns (Delcroix and Henin, 1991). The long-term effect of heavy rainfall together with low heat flux across the sea surface is the creation of a “barrier-layer” (Lukas and Lindstrom, 1991) in the upper ocean which has a haline stratification but is almost isothermal.

Table 3-1 Sea surface salinity accuracy/resolution requirements.

Area	Accuracy	Horiz. Resolution	Temp. Resolution
Coastal process studies	1 psu	20 km	1-10 days
ENSO observation	0.1 psu	100 km	1 month
Assimilation in ocean models	0.1 psu	200 km	10 days
Buoyancy driven Circulation in tropics	0.3 psu	50-100 km	1 day
Polar eddies	0.2 psu	50 km	10 days
Polar front meanders	0.2 psu	100 km	10 days
Freshwater lenses	1psu 0.1 psu	50 km	1 day 10 days
Great salinity anomalies	0.1 psu	100 km	6 months
Calculation of geostrophic velocites	0.5 psu	100 km	10 days

3.2 Salinity variation due to freshwater flux

Freshwater fluxes at the sea surface lead to changes in the surface salinity. These are caused by rainfall and evaporation at the sea surface or by continental river runoff in coastal areas. During rainfall freshwater lenses are produced on the ocean which are stable features as freshwater is less dense than sea water. These lenses mix slowly with the bulk sea water and can persist from hours to weeks depending on wind-speed conditions. Heavy rainfall can cause a drop in surface salinity of 7 psu for short time periods and still 4 psu in hourly averages as measured by Paulson and Lagerloef (1993) in the tropical Pacific Ocean during TOGA/COARE (Tropical Ocean Global Atmosphere Coupled Ocean Atmosphere Response Experiment). The size of single freshwater lenses is of the order 50 to 100 km, depending on the size and lifetime of the convective rain cells as well as their horizontal displacement with time.

On the basis of observations and modelling Brainerd and Gregg (1997) show that freshwater lenses in the western Pacific warm pool have a lifetime of a few days before they are mixed away by convection in the upper ocean that is driven mainly by nighttime cooling. The evolution of a rain-formed freshwater anomaly under the influence of a westerly wind burst in the western equatorial Pacific Ocean has been studied by Wijesekera et al. (1998) by observation and modelling. They report about a lens generated by heavy rainfall (20 mm/h for one-hour duration) that developed under winds of 10 m/s and a surface cooling of 225 W/m^2. Five hours after being formed the low-salinity anomaly had penetrated to a depth of 40 m with a surface magnitude of 0.15 psu. The temperature and salinity fluctuations within the lens were large but highly coherent. Furthermore, their model results indicate that a strong near-surface density stratification in the fresh lenses can cause the momentum from the wind to be trapped near the surface so that a fresh lens becomes a fresh jet.

The horizontal velocity gradients associated with a fresh lens can lead to upwelling near the upwind edge of the lens and downwelling at the downwind edge. Wijesekera et al. (1998) estimate the vertical velocity as 20 to 30 m per day at a depth of 30 m. Advection of freshwater lenses by oceanic currents may lead to salinity anomalies in

(3) Three-dimensional ocean models have to be initialised by including salinity (Cooper, 1988).

(4) One-dimensional models for the description of the upper oceanic mixed layer are to be initialised, inter alia, with salinity profiles in the upper ocean (Price et al., 1986; Anderson et al., 1996).

(5) Surface salinity of the western Pacific is important for the heat content storage, for the propagation of Rossby and Kelvin waves, and for the genesis of the equatorial monsoon jet (Lukas, 1989).

(6) In the tropical regions of the three oceans there is, following historical data, a horizontal salinity boundary layer (Sprintall and Tomczak, 1992).

(7) While ENSO is usually described in terms of sea level and surface temperature changes also the salinity changes during an ENSO cycle and the knowledge of *S* might be crucial for a good model simulation of certain important features of ENSO (Lukas, 1990).

(8) A great salinity anomaly has been observed in the northern North Atlantic between 1968 and 1982. The evolution of this event covered a circuit of more than 10^4 km showing extreme surface salinity anomalies, exceeding –1 psu (Trites, 1982)

(9) Coupled general circulation models need better estimates of freshwater fluxes for their validation and improvement (Delecluse et al., 1998). Salinity measurements could be taken as proxy for these fluxes.

An optimal salinity product suited to match the user needs would be a three-dimensional salinity field of the ocean. However, from the physics involved it is clear that remote sensing techniques would only allow for the retrieval of surface salinity, i.e., the average salinity of a layer as deep as the penetration depth of the radiation used. Possible frequencies are those where the dielectric constant is sufficiently dependent on the salinity. These frequencies are near 1 GHz where the radiation penetrates into the ocean by about 1 cm.

Based on the following sections, a table of accuracy and resolution requirements for sea surface salinity measurements is given in Table 3-1.

In addition, some key chemical properties of sea water is dependent on salinity. For instance, the solubility of the greenhouse gas CO_2 depends on salinity (Weiss, 1974). Spatial and temporal resolved sea surface salinity observations will therefore be useful in studies involving basin to global scale computation of the air-sea flux of CO_2 (e.g., Takahashi et al., 1997). A secondary effect of improved sea surface salinity fields is improved mixed layer dynamics. This is expected to give a better constrained flux of plant nutrients and biomass into and out of the surface layer, and consequently to improved estimates of new production (Dugdale and Goering, 1967).

2 Outline of Report

The report is organised as follows: In Sec. 3, a review of user requirements are given. The section is followed by several investigations of mulitspectral (Sec. 4) and L-band (Sec. 5) retrieval of *S*. In Sec. 6, the importance of *S* in Ocean General Circulation Models is discussed, and summary and recommendations are given in Sec. 7. Finally, Sec. 8 includes an appendix, a list of acronyms, and the reference list.

3 Review of User Requirements

3.1 Background

While satellite measurements of the sea surface and the lower atmosphere have become an integral part of the global observing systems, sea surface salinity *S* has not been monitored from space so far. A sea surface salinity product measured from satellites would be very welcome by several disciplines as the current knowledge about *S* is rather poor. The reason for this is that *in situ* salinity measurements are only scarcely distributed over the oceans. In fact, 1°×1° boxes distributed over the global oceans show that for only about 70% of them a salinity measurement exists at all (Levitus et al., 1994). A far smaller fraction of such areas has been monitored only once. Furthermore, the number of total observations within the grid boxes averages to about 40 only (Lagerloef et al., 1995). This means that the average structures of the surface salinity field are known to some extent, but, details about its variability even on seasonal and interannual scales remain hidden.

The distribution of salt in the global ocean and its annual as well as interannual variability are crucial in understanding the role of the ocean in the climate system. Delcroix and Hénin (1991) summarise: Salt affects the thermohaline circulation and therefore the distribution of mass and heat. Salinity may control the formation of water masses, which allows its use for tracer studies. Salinity is thermodynamically important as salinity stratification can influence the penetration depth of convection at high latitudes and may determine the mixed layer depth in equatorial regions. In tropical areas the salinity is useful as indicator of precipitation and evaporation, thus it is of great interest in studies of surface water fluxes. Knowledge of the salinity distribution is necessary to determine the equation of state. For the calculation of dynamic height anomalies the salinity distribution must be known. Dynamic height variations are used in calculating geostrophic circulation and when using satellite based altimetric measurements (e.g. a 0.5 psu error accounts for 3.8 cm/s error in geostrophic velocity at 1 km depth calculated from the corresponding surface value). Accurate model simulations are only possible when salinity fields are included.

The need for frequent and complete observations of *S* is substantiated by the following reasons which have mostly been reconciled by Donguy (1994):

(1) The surface salinity varies as a consequence of an exchange of water between ocean and atmosphere and continental runoff.

(2) The calculation of the dynamics of geostrophic currents is far more accurate when supplementing the input data (consisting of XBT profiles) with surface salinity data (Kessler and Taft, 1987).

more) to be fully useful. This, together with the fact that the accuracy of remotely sensed S decreases with sea surface temperature T, indicates that high-latitude OS measurements are problematic of nature.

Several retrieval simulations are presented in the report, and the results can be summarised as follows:

Horizontally as well as vertically polarized brightness temperatures T_b must be measured to obtain reasonable retrievals. To make useful measurements of S it is necessary to have at least dual polarized measurements at two frequencies near 1.4 and 6.8 GHz. The inclusion of a channel at 2.65Ghz is useful only if the noise can be reduced to values below 0.2 K. At smaller noise levels one could take advantage of accurate surface temperature and wind speed measurements. The latter are the more important ones. If one could obtain wind speed fields with accuracy better than 0.5 m/s and temperature fields with an accuracy of 0.5 K, then the salinity could be retrieved with an error well below 0.4 psu. It is important that the single measurements have a noise below 0.5 K and an average of more than 100 brightness temperature measurements can be built.

It is shown that the errors in salinity obtained from the performed calculation come close to meeting the GODAE optimised requirements (and definitely meet the threshold requirements). This means that the L-band measurements seem capable of providing useful sea surface salinity data (except in those parts of the ocean where surface water temperature is low).

Furthermore, it is shown that uniform errors in T and T_b give approximately uniform errors in S, and normal errors led to approximately normal errors. Also, the relationship given by T, T_b, and S is only very weakly nonlinear. Consequently, it may be possible to linearise and simplify the relationship between these quantities.

Accurate retrieval of S requires small or no bias in the measurements of the brightness temperature T_b. This has implications for the engineering design and subsequent calibration of an L-band passive microwave salinity sensor.

It is also argued that it is not necessary to have simultaneous measurements of T and T_b to retrieve S to useful accuracy. This is not entirely surprising as mesoscale changes in the ocean occur over periods of 10-30 days, typically. Additionally, averaging T and T_b and then retrieving S seems to lead to results with smaller bias. This suggests that it may be best to simply average non-simultaneous measurements of T and T_b over the period and area of interest before retrieving S.

In terms of meeting the GODAE requirements, the simulations have shown that one can get close to the accuracy of 0.1psu for a 10 day, 200^2 km^2 average. This is encouraging, but there are unaccounted effects that might increase the error, particularly any bias in the measurement of T_b. The ability of a sensor like MIRAS to view the same patch of ocean at several different incidence angles as it flies over an area will increase the number of measurements and therefore decrease the error.

1 Executive Summary

The objective of the project has been to define critical requirements for the retrieval of Ocean Salinity (OS) from space.

The document addresses the need for remotely sensed OS as the available distribution of *in situ* sea surface salinity (*S*) measurements are sparse in time and space. Therefore, the spatial distribution and temporal evolution of the World Ocean *S* field is rather poorly known. Given the crucial role *S* play in determining the general circulation and thermodynamics of the ocean, and any processes that are directly or indirectly effected by the ocean dynamics, it is clear that most of the marine sciences and disciplines will benefit from remotely sensed OS.

The Global Ocean Data Assimilation Experiment (GODAE) gives the following optimised and threshold requirements for sea surface salinity measurements:

	Optimised requirements	Threshold requirements
Spatiol resolution (km)	200	500
Temporal resolution (days)	10	10
Accuracy (psu)	0.1	1.0

These requirements, which should be taken as representative for the Global Ocean, can be compared with the natural spatial and temporal accuracy requirements in the *S* field for the following phenomena

Process/area	Accuracy	Horiz. Resolution	Temp. Resolution
Coastal process studies	1 psu	20 km	1-10 days
ENSO observation	0.1 psu	100 km	1 month
Assimilation in ocean models	0.1 psu	200 km	10 days
Buoyancy driven circulation in tropics	0.3 psu	50-100 km	1 day
Polar eddies	0.2 psu	50 km	10 days
Polar front meanders	0.2 psu	100 km	10 days
Freshwater lenses	1psu 0.1 psu	50 km	1 day 10 days
Great salinity anomalies	0.1 psu	100 km	6 months
Calculation of geostrophic velocites	0.5 psu	100 km	10 days

From these tables it follows that an accuracy of 0.1 psu over a distance of 100 km to 200 km for a time period of about a week is an optimised requirement for description and quantification of many central ocean processes. Given the sparse distribution of *in situ* surface salinity observations, it follows that even the above stated threshold requirement will be useful in extending and improving existing climatologies of *S*.

It should be noted that certain regions (like polar and sub-polar waters) are extremely sensitive to changes in *S*, at least for periods with weak vertical stratification, and that these regions will require an accuracy well below 0.1 psu (by an order of magnitude or

1 EXECUTIVE SUMMARY 4

2 OUTLINE OF REPORT 6

3 REVIEW OF USER REQUIREMENTS 6

3.1 BACKGROUND 6
3.2 SALINITY VARIATION DUE TO FRESHWATER FLUX 8
3.3 RIVER DISCHARGE ON THE CONTINENTAL SHELF 10
3.4 GREAT SALINITY ANOMALIES 10
3.5 UPPER OCEAN SALINITY BOUNDARY CONDITION USED IN MODELS 11
3.6 VARIABILITY OF SURFACE SALINITY IN THE TROPICAL OCEAN RELATED TO ENSO 12
3.7 IMPACT OF SURFACE SALINITY ON NUMERICAL WEATHER FORECAST 14
3.8 ASSIMILATION OF SALINITY IN OCEAN MODELS 14
3.9 REQUIREMENTS OF COMMERCIAL USERS 15

4 VARIATION OF THE RADIATION FIELD DUE TO SALINITY CHANGES AND MULTISPECTRAL RETRIEVAL OF THE SURFACE SALINITY 15

5 RETRIEVAL OF SEA SURFACE SALINITY FROM L-BAND PASSIVE MICROWAVE RADIOMETER MEASUREMENTS 23

5.1 INTRODUCTION 23
5.1.1 Simulating the retrieval of S from L-band brightness temperatures 24
5.1.2 Key to tables of simulation results 26
5.1.3 Discussion and initial conclusions 38
5.2 RETRIEVAL OF *S*: SIMULATIONS USING OCCAM 38
5.2.1 Introduction 38
5.2.2 OCCAM: a brief description 39
5.2.3 Simulation using OCCAM 39
5.2.4 Results and discussion 43
5.2.5 Conclusions 45

6 THE IMPORTANCE OF SEA SURFACE SALINITY IN OCEAN GENERAL CIRCULATION MODELS 45

6.1 OBSERVED, GLOBAL MONTHLY MEAN SURFACE SALINITY FIELDS 46
6.1.1 Spatial and Temporal Evolution of SSS 47
6.1.2 Annual mean SSS field 47
6.1.3 Horizontal gradients in SSS 49
6.1.4 Annual variation in SSS 49
6.1.5 Vertical surface salinity gradients 50
6.1.6 SST and SSS dependency on surface water density 51
6.2 SIMULATED SSS VARIABILITY AND ANOMALIES IN A BASIN SCALE OGCM 52

7 SUMMARY AND RECOMMENDATIONS 55

8 MISCELLANEOUS 57

8.1 ACKNOWLEDGEMENTS 57
8.2 APPENDIX 57
8.3 ACRONYMS 60
8.4 REFERENCES 60

ESA STUDY CONTRACT REPORT

ESA CONTRACT NO	SUBJECT		CONTRACTOR
13224/98/NL/MV	Study of Critical Requirements for Ocean Salinity Retrieval Using a Low Frequency Microwave Radiometer		Nansen Environmental and Remote Sensing Center
ESA CR()No	STAR CODE	No of volumes 1 This is Volume No 1	Contractor's Reference —

ABSTRACT:

A preliminary assessment of the potential of sea surface salinity observations from space-borne microwave radiometer is presented. A literature survey indicates that an accuracy of 0.1 psu (practical salinity units) over a distance of 100 km to 200 km for a time period of about a week is an optimised requirement for description and quantification of many central ocean processes. Given the sparse distribution of *in situ* surface salinity observations, it follows that even a threshold requirement of 1 psu over a distance of 500 km for a time period of about 10 days will be useful in extending and improving existing climatologies.

It is shown that errors in salinity obtained from space-borne microwave radiometer may come close to the optimised requirements, and definitely meet the threshold requirements. This means that a microwave radiometer seems capable of providing useful sea surface salinity values, at least for those parts of the ocean that are characterised by a non-vanishing vertical density stratification.

Names of authors

Helge Drange, Peter Schlüssel, and Meric Srokosz

Reference

Drange, H., P. Schlüssel & M. Srokosz, 1999: Study of Critical Requirements for Ocean Salinity Retrieval Using a Low Frequency Microwave Radiometer. ESA Contract no. 13224/98/NL/MV, Final Report, Keplerlaan 1, 2201 AZ NOORDWIJK, Netherlands (65 pp)

Online available from

http://www.nrsc.no/rieber.html

NAME OF ESA STUDY MANAGER	ESA BUDGET HEADING
J. A. Johannessen DIV: Earth Sciences DIRECTORATE: Science	

Study of Critical Requirements for Ocean Salinity Retrieval Using a Low Frequency Microwave Radiometer

Final Report

(ESA Contract No. 13224/98/NL/MV)

Helge Drange, Nansen Environmental and Remote Sensing Center (NERSC), Edv. Griegsv. 3A, 5037 Solheimsviken, NORWAY;

Peter Schlüssel, Meteorologisches Institut, Universität München, Theresienstrasse 37, 80333 München, GERMANY; and

Meric Srokosz, Southampton Oceanography Centre (SOC), Empress Dock, Southampton, SO14 3ZH, UK